MATERIALS SCIENCE

Toward controllable and predictable synthesis of high-entropy alloy nanocrystals

Yi-Hong Liu[1], Chia-Jui Hsieh[1], Liang-Ching Hsu[2], Kun-Han Lin[1], Yueh-Chun Hsiao[1], Chong-Chi Chi[3], Jui-Tai Lin[1], Chun-Wei Chang[1], Shang-Cheng Lin[1], Cheng-Yu Wu[1], Jia-Qi Gao[1], Chih-Wen Pao[2], Yin-Mei Chang[3], Ming-Yen Lu[3,4], Shan Zhou[5], Tung-Han Yang[1]*

High-entropy alloy (HEA) nanocrystals have attracted extensive attention in catalysis. However, there are no effective strategies for synthesizing them in a controllable and predictable manner. With quinary HEA nanocrystals made of platinum-group metals as an example, we demonstrate that their structures with spatial compositions can be predicted by quantitatively knowing the reduction kinetics of metal precursors and entropy of mixing in the nanocrystals under dropwise addition of the mixing five–metal precursor solution. The time to reach a steady state for each precursor plays a pivotal role in determining the structures of HEA nanocrystals with homogeneous alloy and core-shell features. Compared to the commercial platinum/carbon and phase-separated counterparts, the dendritic HEA nanocrystals with a defect-rich surface show substantial enhancement in catalytic activity and durability toward both hydrogen evolution and oxidation. This quantitative study will lead to a paradigm shift in the design of HEA nanocrystals, pushing away from the trial-and-error approach.

INTRODUCTION

High-entropy alloy (HEA) nanocrystals consisting of at least five elements hold great promise as a family of catalysts owing to the large chemical space and tunability (*1*–*23*). Their potential applications in electrocatalysis, photocatalysis, and thermocatalysis have been widely reported in recent years. The multiprincipal element feature contributes to high mixing entropy and facilitates the formation of solid-solution phase rather than the intermetallic phase or phase-separated mixture (*1*, *2*, *7*–*9*, *20*, *24*–*30*). Compared to conventional mono- and bimetallic nanocrystals (*24*, *30*), HEA nanocrystals can provide unique surfaces exposed by the random distribution of dissimilar elements. They thus have an enormous number of diverse types of active sites and distinct local electronic structures, greatly expanding an immense design space for catalysts with desirable activity, selectivity, and durability. For example, the PdPtRhIrRuOsAgAu HEA nanocrystals marked a high hydrogen evolution reaction (HER) activity with a small overpotential in acid over prolonged operations (*23*). For another example, the PtRuCoNiFeMo HEA nanowires showed excellent mass and specific activities as well as superior durability toward alkaline hydrogen oxidation reaction (HOR) (*15*).

Recently, various synthesis strategies including wet-chemical synthesis (*11*, *15*, *17*, *22*, *23*), thermal annealing treatments (*5*, *9*, *10*, *12*–*14*, *16*, *18*), and laser-assisted methods (*19*) have been demonstrated for the synthesis of diverse HEA nanocrystals with different functionalities. However, current methods generally involve a trial-and-error approach to reaching the optimization of synthetic protocols, which can be attributed to the fact that the experimental parameters continue to be built upon qualitative observations and empirical laws (*31*). The multimetallic nanocrystals can take many distinct types of phases (e.g., solid-solution, intermetallic, and phase-separated alloys) with various spatial composition distributions of constituent elements (e.g., alloy and core-shell structures), which are determined by a large number of intricately entangled experimental parameters (*1*, *2*, *7*–*9*, *20*, *28*–*38*). Because of the distinctive reduction kinetics of metal precursors into atoms for their subsequent nucleation and growth into nanocrystals (*24*, *28*, *29*, *32*, *33*, *35*), it is not an overstatement that conventional trial-and-error approaches are extremely time-consuming and almost impossible to control the outcome of multimetallic synthesis (the so-called "black box"). This is especially problematic in the synthesis of solid-solution HEA nanocrystals containing typically five or more elements. With HEA nanocrystals consisting of five platinum-group metals (PGMs; Pd, Pt, Rh, Ir, and Ru) as an example, here, we demonstrate that their structures with different spatial compositions can be controlled by the quantitative understanding of the reduction kinetics of the metal precursors and entropy of mixing in the nanocrystals as a function of reaction time during the dropwise synthesis. We select the five elements of PGMs because each element could promote unique catalytic reactions, and, thus, alloying these elements into the solid-solution HEA nanocrystals may provide a great variety of adsorption sites on their surfaces for various catalyses (*11*). In addition, the PGMs are the neighboring elements in the periodic table and have similar atomic radii, which could facilitate the homogeneous random elemental mixing for the formation of HEA nanocrystals. Our kinetic analysis suggests that the time to reach a steady state of precursor ions for each precursor plays a key role in the formation of three distinctive HEA nanocrystals including the typical PdPtRhIrRu nanocrystals, dendritic PdPtRhIrRu nanocrystals, and Pd@PdPtRhIrRu core-shell nanocrystals. In addition, the compositional stoichiometry within PdPtRhIrRu nanocrystals also can be tuned by adjusting the ratios of metal precursors added to the

[1]Department of Chemical Engineering, National Tsing Hua University, Hsinchu 30013, Taiwan. [2]National Synchrotron Radiation Research Center, Hsinchu 30076, Taiwan. [3]Instrumentation Center, National Tsing Hua University, Hsinchu 30013, Taiwan. [4]Department of Materials Science and Engineering, National Tsing Hua University, Hsinchu 30013, Taiwan. [5]Department of Nanoscience and Biomedical Engineering, South Dakota School of Mines and Technology, Rapid City, SD 57701, USA.
*Corresponding author. Email: tunghanyang@mx.nthu.edu.tw

synthesis, giving rise to the expanded design space for catalysts. When benchmarked against the commercial Pt/C and phase-separated nanocrystals, the obtained PtPdRhIrRu HEA nanocrystals have high catalytic activity and durability toward electrocatalytic HER and HOR.

RESULTS

One-pot synthesis of phase-separated multimetallic nanocrystals

We first conducted the one-pot synthesis to examine whether the one-shot injection of the precursor solution instead of dropwise addition would obtain solid-solution HEA nanocrystals. Because of the different reduction kinetics of metal precursors and thus sequential generations of atoms, it is expected that the one-pot synthesis will induce the formation of phase-separated nanocrystals. Before the synthesis, we studied the reduction kinetics of five metal precursors [i.e., Pd(II), Pt(II), Rh(III), Ir(IV), and Ru(III)] of PGMs. In the kinetic measurements, 3.0 ml of ethylene glycol (EG) precursor solution including five different types of metal precursors in an equimolar ratio was introduced in one shot into a preheated 7.0-ml EG reaction solution containing L-ascorbic acid (AA; reductant) and poly(vinylpyrrolidone) (PVP; colloidal stabilizer) at a temperature of 180°C. We measured the concentrations of precursor ions remaining in the reaction solution at different time points for five metal precursors using the inductively coupled plasma optical emission spectrometry (ICP-OES) (fig. S1, A to E). We then derived their reduction rate constants k by the curve fittings based on the pseudo–first-order rate law (fig. S1, F to J) (*28*, *29*, *31*–*35*). The rate constants were determined to be 6.50×10^{-2}, 3.18×10^{-2}, 5.29×10^{-3}, 2.28×10^{-3}, and 1.04×10^{-3} s^{-1} for the reduction of Pd(II), Pt(II), Rh(III), Ir(IV), and Ru(III), respectively, suggesting that the reduction kinetics of precursors followed the trend of Pd(II) > Pt(II) > Rh(III) > Ir(IV) > Ru(III) (table S1). On the basis of these kinetic parameters, we derived the number of metal precursor ions remaining in the reaction solution as a function of reaction time, as shown in Fig. 1A. As highlighted in the inset of Fig. 1A, 99.0% of the Pd(II) precursor will be reduced to Pd atoms within 1 min, which is much faster than those of the other four precursors. We also calculated the instantaneous percentages of Pd, Pt, Rh, Ir, and Ru atoms generated as a function of reaction time, as shown in Fig. 1B. The percentage of Pd atoms will dominate among these five elements in the early stage of synthesis, followed by the Pt, Rh, Ir, and Ru atoms as the reaction proceeds. Furthermore, we estimated the instantaneous entropy of mixing (ΔS_{mix}) as a function of reaction time using the following equation (*1*, *2*, *8*, *39*)

$$\Delta S_{mix} = -R \sum_{i=1}^{n} x_i \ln x_i \quad (1)$$

where R is the gas constant, X_i the molar fraction of the ith element, and n denotes the number of elemental components in the alloys. According to the calculation of the ΔS_{mix}, alloys can be divided into low ($\Delta S_{mix} < 1R$), medium ($1R \leq \Delta S_{mix} \leq 1.5R$), and HEAs ($\Delta S_{mix} > 1.5R$) (*39*). As shown in Fig. 1C, the ΔS_{mix} showed a rapid increase after the one-shot injection of precursor solution and decreased markedly later on. The values are much smaller than $1.5R$ throughout the synthesis, resulting in a high probability of forming phase-separated multimetallic nanocrystals.

Figure 1 (D to H) shows the transmission electron microscopy (TEM) and high-angle annular dark-field scanning TEM (HAADF-STEM) images of the resultant multimetallic PdPtRhIrRu nanocrystals with two distinct sizes and shapes from the one-pot synthesis. The larger nanocrystals exhibited islands or spikes distributed on the surface (Fig. 1, E and F). The fast Fourier transform (FFT) pattern in the inset of Fig. 1F showed the single-crystal face-centered cubic (FCC) structure, which was also confirmed by x-ray diffraction (XRD) pattern (fig. S2). We further analyzed these nanocrystals by energy-dispersive x-ray spectroscopy (EDS) mapping to examine the element distribution. As shown in Fig. 1I, the Pd-rich region in the core area and the other four Pt, Ir, Rh, and Ru elements in the outer surface were observed, respectively, indicating the nonuniform elemental distribution. Apart from the larger nanocrystals, there were many tiny clusters and wavy nanowires with a diameter as thin as ~2 nm (Fig. 1, G and H). The nanowires were generated from the aggregation of tiny clusters. The FFT pattern in the inset of Fig. 1H shows a typical polycrystalline diffraction pattern and the lattice constant (0.23 nm) calculated from the first diffraction ring matches that of FCC (111) plane. Elemental mapping based on EDS (Fig. 1J) confirmed that the wavy nanowires were only composed of the four Pt, Rh, Ir, and Ru elements. These above results suggest that the phase-separated multimetallic nanocrystals were obtained, which is consistent with our quantitative results. The numerous Pd atoms formed from the Pd(II) reduction within a short time underwent nucleation and growth to generate nanocrystals, and, subsequently, the atoms from the other precursors [i.e., Pt(II), Rh(III), Ir(IV), and Ru(III)] with slower reduction kinetics can be deposited on the just-formed Pd nanocrystals, leading to the formation of phase-separated multimetallic nanocrystals with the Pd-rich core and Pt, Rh, Ir, and Ru shell (Fig. 1, E and F). In addition, the number of nucleation sites provided by the just-formed Pd nanocrystals is not sufficiently large to accommodate all the four Pt, Rh, Ir, and Ru atoms. These four atoms can also undergo nucleation and growth to generate clusters/nanowires (Fig. 1, G and H). In addition, we obtained the phase-separated PdPtRhIrRu nanocrystals as the products using different reaction temperatures of 140°, 160°, and 200°C through the one-pot synthesis (fig. S3, A to F).

Dropwise synthesis of solid-solution HEA nanocrystals

We then switched to the use of the dropwise synthesis to introduce the precursor solution dropwise into the reaction solution through the assistance of a syringe pump for the synthesis of solid-solution HEA nanocrystals, while all other experimental conditions were kept the same. The detailed experimental procedures are provided in the experimental section. We argue that the dropwise strategy can provide an opportunity to simultaneously reach a steady state for the number of each metal precursor in the reaction solution. This may allow us to tightly control the number of atoms generated from the different types of precursors at the same value in the time interval between adjacent drops during the steady state, followed by their nucleation and then growth into HEA nanocrystals. To quantitatively understand the reduction kinetics of metal precursors in the dropwise synthesis, we combined the kinetic measurements and mathematical analysis. The number of metal precursor ions (n_t) remaining in the reaction solution at reaction time t can be

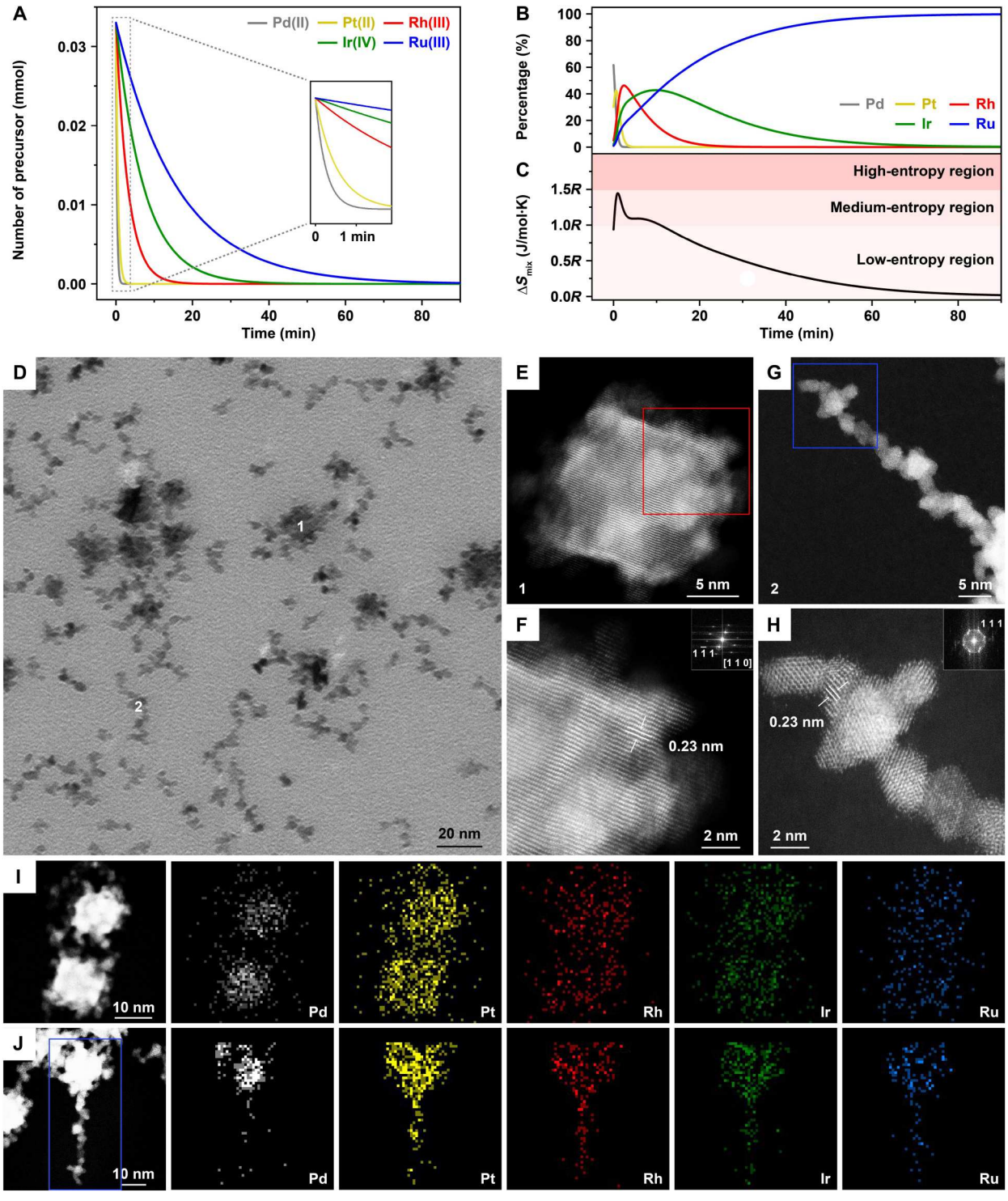

Fig. 1. One-pot synthesis of phase-separated multimetallic nanocrystals. (**A**) The numbers of Pd(II), Pt(II), Rh(III), Ir(IV), and Ru(III) ions remaining in the reaction solution, (**B**) the instantaneous percentages of Pd, Pt, Rh, Ir, and Ru atoms generated, and (**C**) the instantaneous entropy of mixing ΔS_{mix} as a function of reaction time. (**D**) TEM image of phase-separated PdPtRhIrRu nanocrystals with two distinct sizes and shapes. (**E**) HAADF-STEM image of a larger phase-separated PdPtRhIrRu nanocrystal. (**F**) Atomic-resolution HAADF-STEM image taken from the region marked by box in (E). (**G**) HAADF-STEM image of a smaller phase-separated PdPtRhIrRu nanowire. (**H**) Atomic-resolution HAADF-STEM image taken from the region marked by box in (G). (**I** and **J**) EDS maps of Pd, Pt, Rh, Ir, and Ru elements of (I) larger phase-separated PdPtRhIrRu nanocrystals and (J) smaller phase-separated PdPtRhIrRu nanowires marked by box.

calculated as a sum of contributions from all drops (*32*)

$$n_t = n_0 e^{-kt} + n_0 e^{-k(t-\tau)} + n_0 e^{-k(t-2\tau)} + \cdots + n_0 e^{-k(t-N\tau)} = \frac{n_0 e^{-kt} \times [1-(e^{k\tau})^{N+1}]}{1-e^{k\tau}} \quad (2)$$

where n_0 is the number of metal precursor ions in each drop, τ represents the duration of time between adjacent drops, k is the reduction rate constant, and N represents the total number of droplets added. On the basis of this equation, the steady state for the number of precursor ions can be manipulated by controlling three variables, including n_0, τ, and k. The values of n_0 and τ can be controlled by adjusting the precursor concentration and injection rate, respectively, while k can be derived experimentally from the kinetic measurements (fig. S1).

After obtaining the rate constants from the kinetic analysis, the number of each metal precursor as a function of the reaction time (Fig. 2A) can be estimated using Eq. 2 when n_0 and τ were set to 1.045×10^{-4} mmol and 68.4 s, respectively. All the Pd(II) and Pt(II) ions (i.e., n_0) will have been reduced to zerovalent atoms under fast reduction kinetics and thus depleted before the next drop is added, as highlighted in the inset of Fig. 2A, suggesting the achievement of steady state for the numbers of Pd(II) and Pt(II) ions. For the Rh(III), Ir(IV), and Ru(III) ions with slow reduction kinetics, these precursor ions will be gradually accumulated in the reaction solution when the number of drops is increased. Then, the numbers of the Rh(III), Ir(IV), and Ru(III) ions will reach the steady state, where they only oscillate between a lower limit ($\frac{n_0 e^{-k\tau}}{1-e^{-k\tau}}$) and an upper limit ($\frac{n_0}{1-e^{-k\tau}}$), at approximately 12, 27, and 80 min, respectively. In this case, once every drop of the precursor mixture is added during the steady state, the number of the precursor ions will quickly increase from n_{low} to n_{up} and, subsequently, show an exponential decay from n_{up} to n_{low} in the pseudo–first-order reaction until the next drop is added. Note that the difference between n_{up} and n_{low} is n_0. On the basis of the quantitative analysis, all these five precursors can simultaneously maintain the steady state during a long period of synthesis from t = 80 min to 6 hours, as highlighted in the inset of Fig. 2A, indicating that the Pd, Pt, Rh, Ir, and Ru atoms will be generated equally (i.e., n_0). Furthermore, the instantaneous percentages of Pd, Pt, Rh, Ir, and Ru elements generated as a function of reaction time also indicate that these five elements can be gradually changed to an equimolar ratio of approximately 20% after 80 min (Fig. 2B). As expected, the instantaneous entropy of mixing ΔS_{mix} increases larger than $1.5R$ within a very short period (~10 min), once the precursor solution is added dropwise (Fig. 2C). The larger ΔS_{mix} may contribute to the formation of stable solid-solution PdPtRhIrRu nanocrystals (*39*).

Figure 2D shows a TEM image of the resultant HEA PdPtRhIrRu nanocrystals with a narrow size distribution at 180°C for 6 hours through the dropwise synthesis, where n_0 and τ were set to 1.045×10^{-4} mmol and 68.4 s, respectively. The products contained a mixture of tetrahedral and irregularly shaped nanocrystals. The HAADF-STEM image taken from an individual tetrahedron is shown in Fig. 2E. The lattice spacing of 0.23 nm can be assigned to the (111) plane of FCC lattice. The corresponding FFT pattern in the inset of Fig. 2E further confirms a characteristic FCC single-crystal structure viewed from the [110] direction. In addition, the dark bright contrast throughout the nanocrystal was observed, which can be attributed to the difference in atomic weight between these five elements. As shown in Fig. 2F, the HAADF-STEM image and the corresponding FFT pattern of an individual irregular nanocrystal revealed its polycrystalline FCC structure. The XRD pattern in Fig. 2G exhibits two notable peaks at 2θ = 41.1° and 47.2°, corresponding to FCC (111) and (200) planes, respectively. As shown in Fig. 2H, the EDS maps depict homogeneous distributions of all five elements in the nanocrystals. In addition, the ICP-OES results reveal that the atomic percentages of Pd, Pt, Ir, Rh, and Ru elements were 21.7, 21.2, 20.7, 18.0, and 18.4%, respectively, which is consistent with our quantitative prediction (fig. S4). To analyze the surface states of HEA PdPtRhIrRu nanocrystals, x-ray photoelectron spectroscopy (XPS) characterization was conducted. In the binding energy region of 55 to 85 eV (Fig. 2I), the two notable Pt 4f peaks were observed at 71.1 and 74.5 eV, which can be assigned to Pt $4f_{7/2}$ and Pt $4f_{5/2}$ of Pt metal, respectively, while the Ir 4f spectrum shows two peaks at 60.5 and 63.5 eV, corresponding to Ir $4f_{7/2}$ and Ir $4f_{5/2}$ of Ir metal, respectively. In the binding energy region of 275 to 350 eV (Fig. 2J), the 3d doublets from Ru, Rh, and Pd were observed along with the weak Pt 4d and Ir 4d signals. The peak profiles of these five elements in the XPS spectra are all in line with their bulk metals, suggesting the metallic nature of the quinary PdPtRhIrRu HEA nanocrystals (*40*).

Together, these quantitative analyses and experimental results demonstrate that the dropwise synthesis is effective for the synthesis of solid-solution PdPtRhIrRu nanocrystals. It should be pointed out that these nanocrystals should contain the tiny core that is rich in PdPt alloy formed in the very early stage of synthesis and the thick solid-solution PdPtRhIrRu shell generated in the relatively long, later steady-state period (Fig. 2B). We thus simply use "solid-solution PdPtRhIrRu nanocrystals" rather than core-shell nanocrystals throughout this paper, to reflect their major phase and structure in this case. Furthermore, we also showed that the compositional stoichiometry within solid-solution PdPtRhIrRu nanocrystals can be tuned by adjusting the ratios of metal precursors added to the synthesis (figs. S5 and S6). For example, the nonequimolar Pt-rich PdPtRhIrRu HEA nanocrystals were obtained by increasing the feeding ratio of Pt(II) in the precursor solution (fig. S6).

Dropwise synthesis of dendritic solid-solution HEA nanocrystals

Controlling the surface structure of HEA while improving the utilization efficiency of the atoms is also a subject of great importance for catalytic applications. Specifically, various nanodendrites consisting of a dense array of metal branches (e.g., Pt- and Pd-based metals and alloys) with low-coordination surface atoms were found to display high catalytic activities (*41*–*44*). It is believed that the growth mode (layer-by-layer versus island growth modes) of metal atoms on the newly formed nuclei (or seeds) can be manipulated by changing the ratio between the atom deposition rate (R_{dep}) and the surface diffusion rate (R_{diff}) (*44*). To facilitate the island growth mode and thus the formation of dendrites, the atom deposition rate needs to be greater than the surface diffusion rate (i.e., $R_{dep} > R_{diff}$). Therefore, we shorten the duration of time between adjacent drops from τ = 68.4 to 11.4 s and, thus, higher R_{dep} by increasing the injection rate of precursor solution to obtain the dendritic solid-solution PdPtRhIrRu nanocrystals in the dropwise synthesis of 180°C, while keeping $n_0 = 1.045 \times 10^{-4}$ mmol. On the basis of reduction rate constants obtained experimentally at 180°C (fig. S1, F to J), we simulated the reduction kinetics under the values of $n_0 = 1.045 \times 10^{-4}$ mmol and τ = 11.4 s to estimate

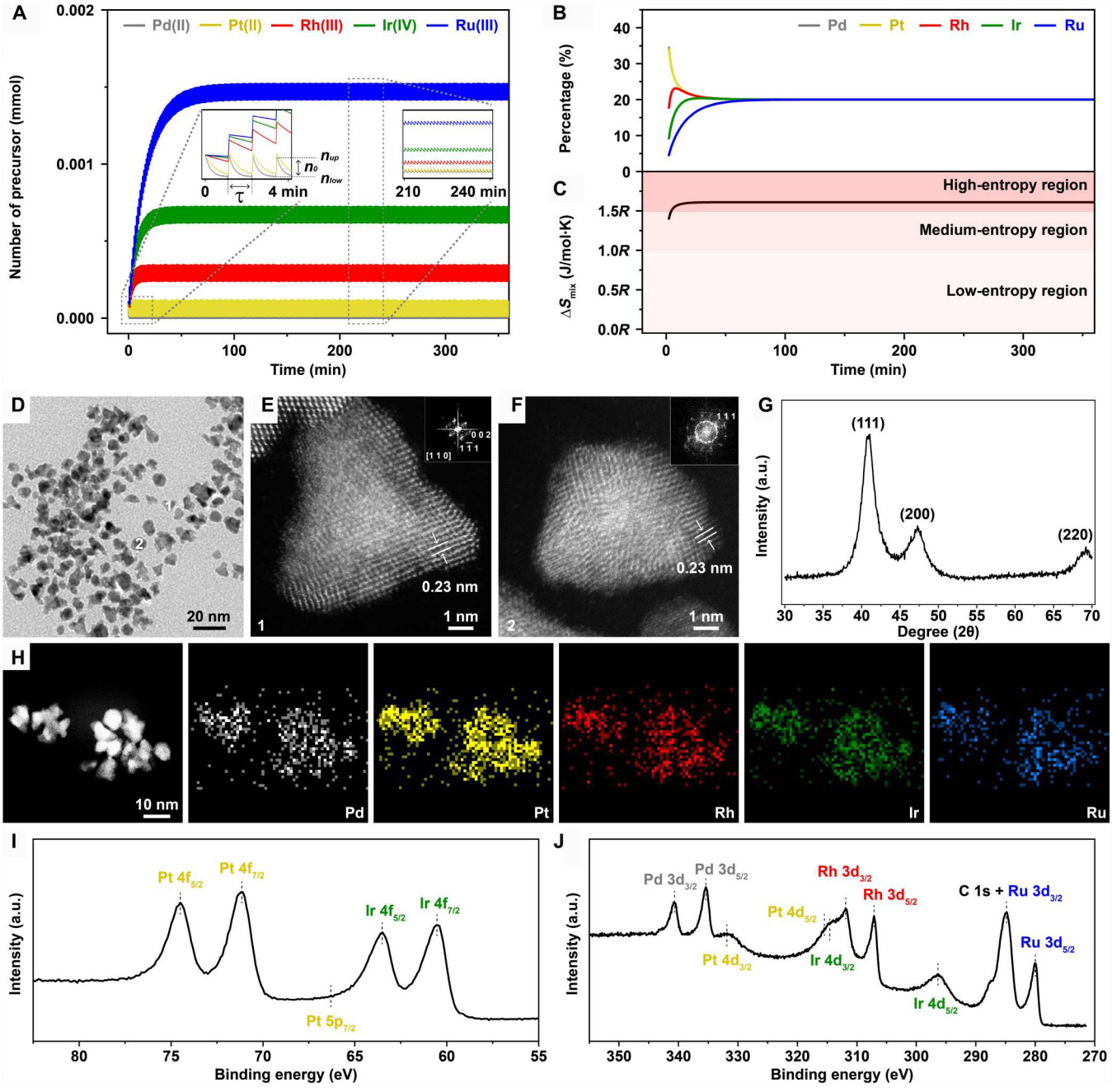

Fig. 2. Dropwise synthesis of solid-solution HEA nanocrystals. (**A**) The numbers of Pd(II), Pt(II), Rh(III), Ir(IV), and Ru(III) ions remaining in the reaction solution, (**B**) the instantaneous percentages of Pd, Pt, Rh, Ir, and Ru atoms generated, and (**C**) the instantaneous entropy of mixing ΔS_{mix} as a function of reaction time. (**D**) TEM image of PdPtRhIrRu nanocrystals. (**E**) Atomic-resolution HAADF-STEM image and its FFT pattern (inset) of a tetrahedral PdPtRhIrRu nanocrystal. (**F**) Atomic-resolution HAADF-STEM image and its FFT pattern (inset) of an irregular PdPtRhIrRu nanocrystal. (**G**) XRD pattern of PdPtRhIrRu nanocrystals. a.u., arbitrary units. (**H**) EDS maps of Pd, Pt, Rh, Ir, and Ru elements of PdPtRhIrRu HEA nanocrystals. (**I** and **J**) XPS spectra of PdPtRhIrRu nanocrystals in the regions of (I) 55 to 85 eV and (J) 275 to 350 eV.

the number of each metal precursor using Eq. 2. Figure 3A shows that the number of each metal precursor all reached a steady state within 80 min. The decrease in τ effectively increased the number of oscillations between a lower limit n_{low} and an upper limit n_{up} in the steady state and thereby increased the atom deposition rate. As shown in Fig. 3B, the instantaneous percentages of five elements formed as a function of reaction time again can be estimated, suggesting that their percentages are approximately the same after a short period of reaction time. Furthermore, the calculated instantaneous entropy of mixing $\Delta S_{mix} > 1.5R$ after ~10 min (Fig. 3C) may facilitate the alloying process for dendritic solid-solution HEA nanocrystals. Figure 3 (D and E) shows the TEM and HAADF-STEM images of dendritic solid-solution PdPtRhIrRu nanocrystals when the dropwise synthesis with $n_0 = 1.045 \times 10^{-4}$ mmol and τ =

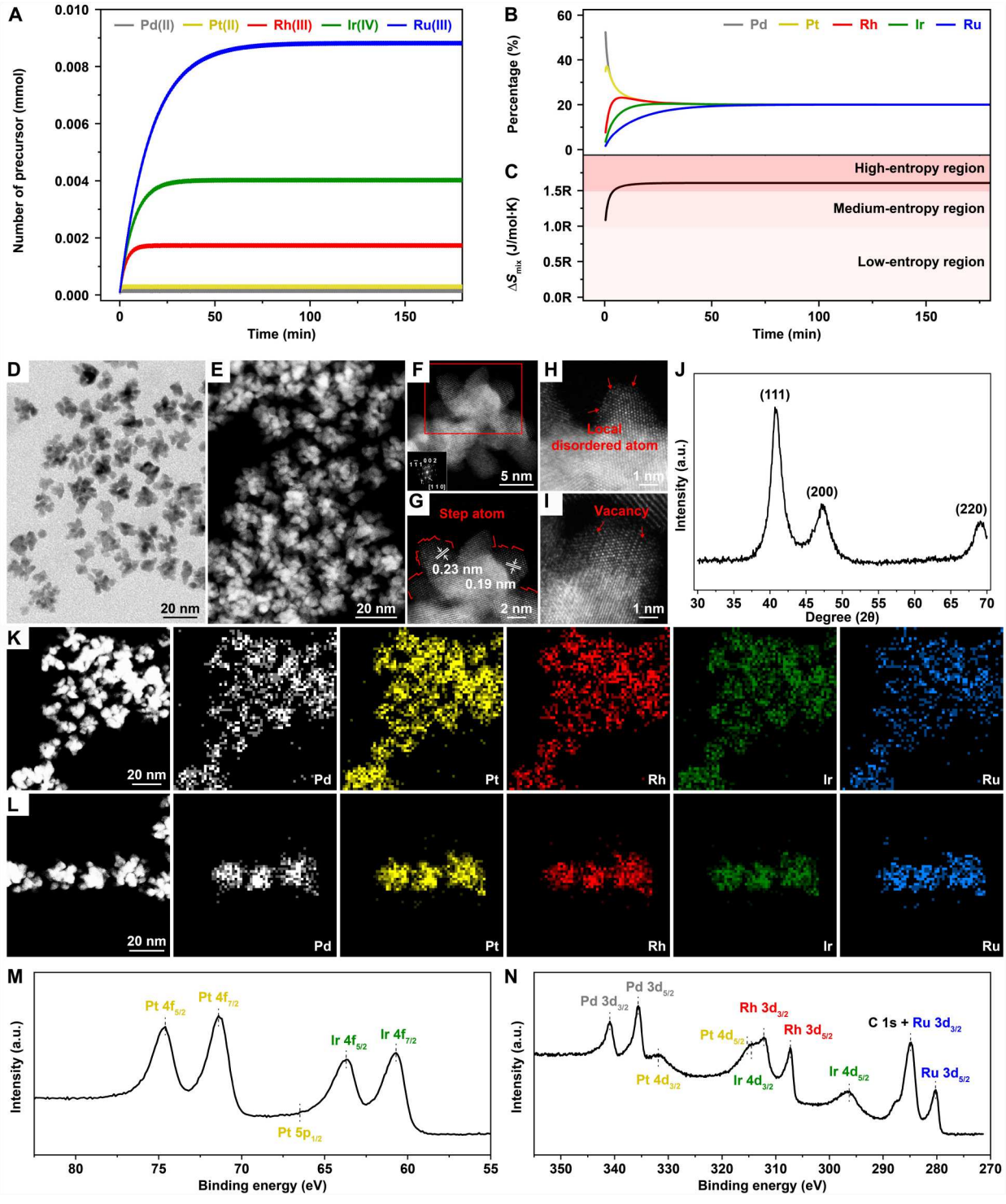

Fig. 3. Dropwise synthesis of dendritic solid-solution HEA nanocrystals. (**A**) The numbers of Pd(II), Pt(II), Rh(III), Ir(IV), and Ru(III) ions remaining in the reaction solution, (**B**) the instantaneous percentages of Pd, Pt, Rh, Ir, and Ru atoms generated, and (**C**) the instantaneous entropy of mixing ΔS_{mix} as a function of reaction time. (**D**) TEM and (**E**) low-magnification HAADF-STEM images of dendritic PdPtRhIrRu nanocrystals. (**F**) HAADF-STEM image of an individual dendritic PdPtRhIrRu nanocrystal. (**G**) Atomic-resolution HAADF-STEM image taken from the region marked by box in (F). (**H** and **I**) Atomic-resolution HAADF-STEM images of PdPtRhIrRu nanocrystals showing the low-coordination defect sites on the nanocrystals. (**J**) XRD pattern of dendritic PdPtRhIrRu nanocrystals. (**K**) Low- and (**L**) high-magnification EDS maps of Pd, Pt, Rh, Ir, and Ru elements of dendritic PdPtRhIrRu nanocrystals. (**M** and **N**) XPS spectra of dendritic PdPtRhIrRu nanocrystals in the regions of (M) 55 to 85 eV and (N) 275 to 350 eV.

11.4 s was conducted at 180°C for 1 hour, respectively. The PdPtRhIrRu nanocrystals had a three-dimensional dendritic morphology consisting of several branches. With the increase in injection time to 3 hours, the structure of dendritic nanocrystals was well maintained and evolved into a larger size (fig. S7). The dendritic nanocrystals sampled at 1 hour were further characterized by atomic resolution HAADF-STEM to observe the lattice details. As shown in Fig. 3 (F to I), the dendritic nanocrystals contained many step atoms (Fig. 3G), local disordered atoms (Fig. 3H), and vacancy defects (Fig. 3I), revealing the abundance of low-coordination defect sites on the surface. The FFT pattern in the inset of Fig. 3F shows at least two sets of FCC diffraction features, suggesting the polycrystalline structure of dendritic nanocrystals. In addition, the FCC structure of dendritic nanocrystals was confirmed by the XRD pattern (Fig. 3J). The low and high magnification EDS maps revealed the random and homogeneous distributions of Pd, Pt, Rh, Ir, and Ru elements in each dendrite nanocrystal, as Fig. 3 (K and L), respectively. The atomic percentages of Pd, Pt, Ir, Rh, and Ru were 22.8, 21.9, 20.2, 18.4, and 16.7%, respectively, which was confirmed by the ICP-OES analysis, consistent with our kinetic analysis (fig. S8). In addition, as shown in Fig. 3 (M and N), the XPS results suggested that the dendritic nanocrystals were in the metallic state.

Furthermore, ex situ x-ray absorption spectroscopy (XAS) was used to acquire the atomic information about the dendritic solid-solution PdPtRhIrRu nanocrystals, as well as the electronic interactions among the five elements. The x-ray absorption near-edge structure (XANES) results of the Pd, Pt, Rh, Ir, and Ru elements in the representative dendritic solid-solution PdPtRhIrRu HEA nanocrystals, and their reference metallic foils and oxides were studied (Fig. 4 and fig. S9). The similarity of the absorption edges of all elements in the HEA nanocrystals with their corresponding foils confirms that the elements were in the metallic state, consistent with the above XPS analysis. In addition, the post-edges of the mixed elements in the HEA nanocrystals exhibited slight deviations in the shape, intensity, and oscillation behavior when compared with the foil references, suggesting the redistribution of electrons among the five elements and distinct orbital hybridizations of the HEA nanocrystals (*13*, *18*, *45*). These features indicated the formation of a solid-solution PdPtRhIrRu HEA phase with the fine-tuning electronic structure. Furthermore, the coordination environments of the mixed elements in the HEA nanocrystals were investigated using the extended x-ray absorption fine structure (EXAFS) spectra, as shown in Fig. 4F. The EXAFS spectra of the mixed elements showed the overlapping of the characteristic peaks owing to the atomic interactions between the constituent elements. In addition, the radial distances of the 4d elements (i.e., Pd, Rh, and Ru) in the HEA nanocrystals were slightly shorter than those of the 5d elements (i.e., Pt and Ir) because of their smaller atomic radii. The radial distances of the 4d and 5d mixed elements also showed distinct differences in comparison to their corresponding metallic foils (fig. S9). The radial distances of the 4d elements in the HEA nanocrystals became longer than those of the foil counterparts (fig. S9, A, C, and E). In contrast, the radial distances of the 5d elements in the HEA nanocrystals were shorter compared to their metallic foils (fig. S9, B and D). The atomic information revealed by ex situ XAS analysis indicated the formation of high-entropy atomic mixing rather than elemental segregation into pure metals, which would display the same length as their metallic foils (*13*, *18*, *45*). Together, these results demonstrated the formation of solid-solution PdPtRhIrRu nanocrystals with a dendritic architecture by shortening the duration of time between adjacent drops. As the control experiments with larger values of τ = 114.0 and 273.5 s, slower injection rates and thus deposition rates induced the nanocrystals with a smooth surface (fig. S10). In addition, when the synthesis with τ = 11.4 s was switched at an elevated temperature of 200°C, the nanocrystals showed less dendritic morphology, which was attributed to a higher diffusion rate at 200°C (fig. S11).

Dropwise synthesis of Pd@HEA core-shell nanocrystals

It is expected that the increasing gaps between the time to reach the steady state for the Pd and the other four Pt, Rh, Ir, and Ru precursors will result in the formation of Pd@PdPtRhIrRu core-shell nanocrystals. To prove the prediction, the dropwise synthesis involves the use of KBr to manipulate the reduction kinetics by influencing the redox potentials of metal precursor ions via ligand exchange at 140°C. This synthetic protocol will allow us to enlarge the rate constant ratios of Pd to the other four Pt, Ir, Rh, and Ru precursors and, thus, enlarge the gap to obtain the steady state. As shown in fig. S12 (A to E), we extended the kinetic measurements for five metal precursors of PGMs in the presence of KBr at 140°C. The rate constants for the reduction of Pd(II), Pt(II), Rh(III), Ir(IV), and Ru(III) were derived as 9.57×10^{-3}, 9.55×10^{-4}, 4.03×10^{-4}, 1.50×10^{-4}, and 5.03×10^{-5} s^{-1} using pseudo–first-order rate law, respectively (fig. S12, F to J, and table S1). The ratios of rate constants between Pd(II)/Pt(II), Pd(II)/Rh(III), Pd(II)/Ir(IV), and Pd(II)/Ru(III) were changed to 10.0, 23.7, 63.8, and 190.3, respectively, which were much larger than those (i.e., 2.0, 12.3, 28.5, and 62.5, respectively) of the kinetic measurements performed in the absence of KBr at 180°C (fig. S1, F to J). Note that it is insufficient to only decrease the reaction temperature to 140°C without the introduction of Br^- ions used to enlarge the ratios of rate constants (figs. S13 and S14 and table S1), suggesting that Br^- ions have a substantial impact on the reduction kinetics of these five Cl^--containing precursor complexes owing to the ligand exchange between Br^- and Cl^- (*28*, *31*).

Again, on the basis of reduction rate constants determined experimentally (fig. S12, F to J), the number of each metal precursor in the dropwise synthesis can be calculated using Eq. 2 when the dropwise synthesis with $n_0 = 1.045 \times 10^{-4}$ mmol and τ = 273.5 s was conducted in the presence of Br^- ions at 140°C for 24 hours, as shown in Fig. 5A. The number of Pd(II) precursor ions reached a steady state after the first few drops. In contrast to the fast kinetics of Pd(II) precursor, the time to the achievement of steady state for Pt(II), Rh(III), and Ir(IV) precursors was extended to 0.8, 3.5, and 6.7 hours, respectively. In addition, Ru(III) precursor was accumulated with the increase in reaction time, and, eventually, the consumption of precursor from each drop reached approximately 98.7% of n_0 at 24 hours, approaching the steady state. These quantitative results suggest that the increase in gaps between the times to reach the steady state was obtained. Again, both the instantaneous percentages of five elements (Fig. 5B) and the instantaneous entropy of mixing ΔS_{mix} (Fig. 5C) as a function of reaction time can be acquired. On the basis of these calculations, the Pd element is expected to dominate the elemental composition of the core formed in the early stage of synthesis, and then all five elements will result in the formation of the PdPtRhIrRu HEA shell in the later steady-state stage.

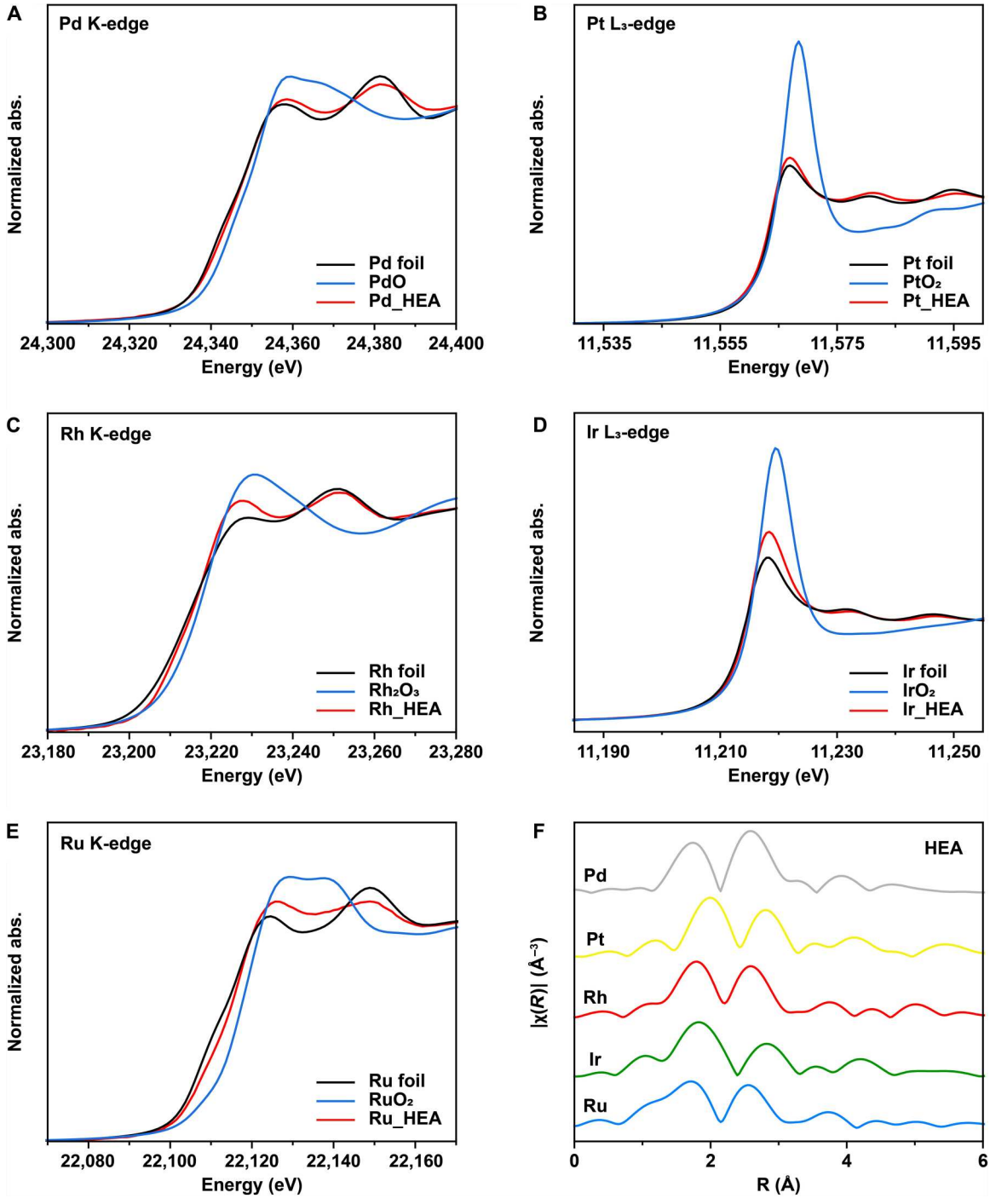

Fig. 4. The coordination structure and electronic structure of dendritic solid-solution PdPtRhIrRu HEA nanocrystals characterized by ex situ XAS analysis. The corresponding metallic foils and oxides were also compared. (**A** to **E**) XANES spectra for the (A) Pd K-edge, (B>) Pt L_3-edge, (C) Rh K-edge, (D) Ir L_3-edge, and (E) Ru K-edge. (**F**) EXAFS spectra for all five elements in the dendritic solid-solution PdPtRhIrRu HEA nanocrystals. abs, absorption.

Figure 5D shows a TEM image of the resultant Pd@PdPtRhIrRu core-shell nanocrystals containing concave tetrahedra and octahedra, as well as irregularly shaped nanocrystals. Figure 5E gives a HAADF-STEM image of a single Pd@PdPtRhIrRu concave core-shell tetrahedron, showing the intense contrast between the Pd core and PdPtRhIrRu shell. The atomic-resolution HAADF-STEM images of the corner (Fig. 5F) and side (Fig. 5, G and H) of the concave tetrahedron were captured. The atomic-resolution HAADF-STEM image (Fig. 5F) taken from the corner of the concave tetrahedron and the relevant FFT pattern viewed from the [110] direction showed the formation of an FCC structure, consistent with the XRD analysis (fig. S15). The observed ($\bar{2}20$) lattice

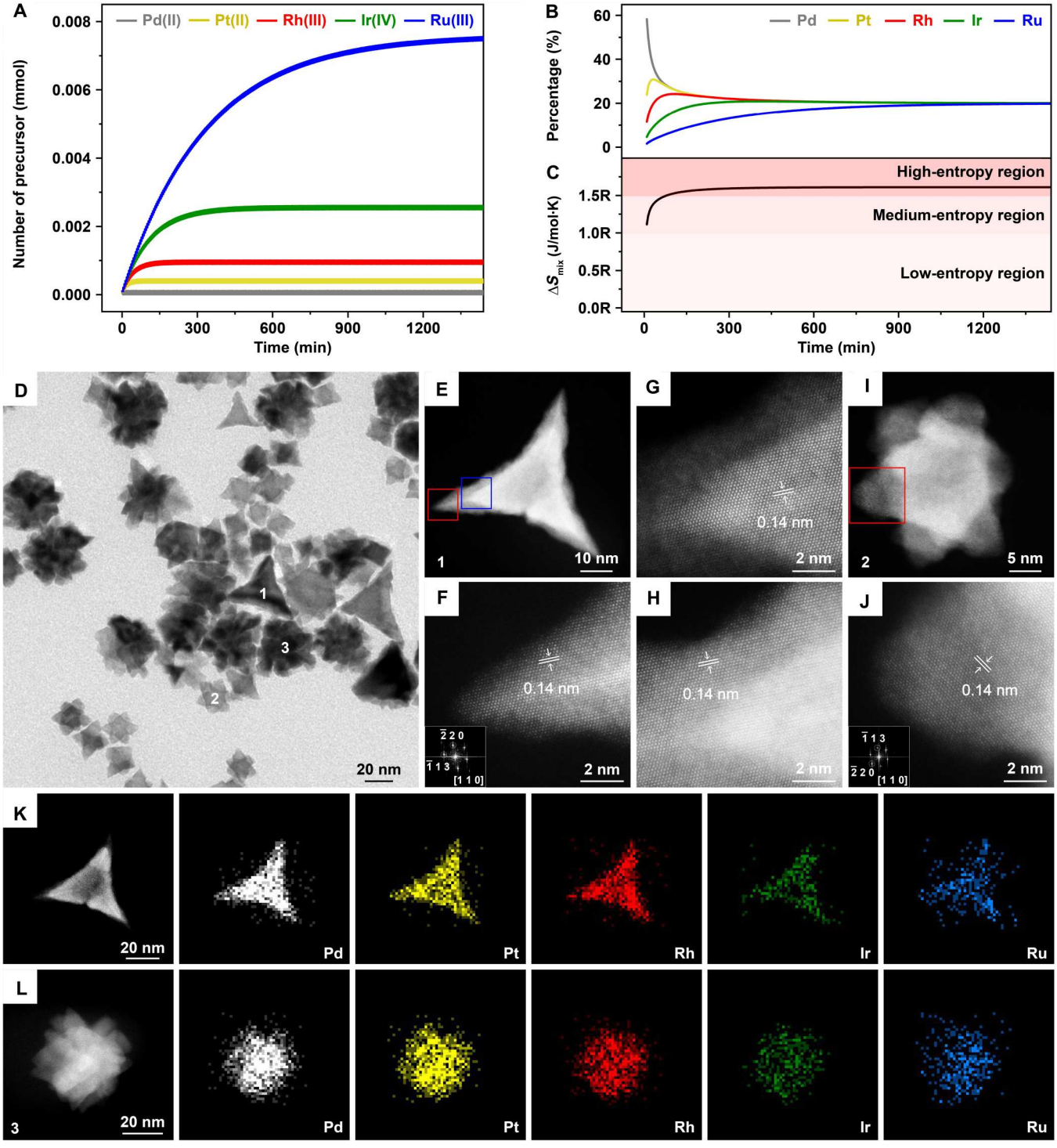

Fig. 5. Dropwise synthesis of Pd@HEA core-shell nanocrystals. (**A**) The numbers of Pd(II), Pt(II), Rh(III), Ir(IV), and Ru(III) ions remaining in the reaction solution, (**B**) the instantaneous percentages of Pd, Pt, Rh, Ir, and Ru atoms generated, and (**C**) the instantaneous entropy of mixing ΔS_{mix} as a function of reaction time. (**D**) TEM image of Pd@PdPtRhIrRu core-shell nanocrystals. (**E**) HAADF-STEM image of an individual Pd@PdPtRhIrRu concave core-shell tetrahedron. (**F**) Atomic-resolution HAADF-STEM image taken from the corner region marked by red box in (E). (**G** and **H**) Atomic-resolution HAADF-STEM images taken from the interior (focus on the core) and exterior (focus on the shell) at the side region marked by blue box in (E). (**I**) HAADF-STEM image of individual Pd@PdPtRhIrRu concave core-shell octahedron. (**J**) Atomic-resolution HAADF-STEM image taken from the region marked by box in (I). (**K** and **L**) EDS maps of Pd, Pt, Rh, Ir, and Ru elements of individual Pd@PdPtRhIrRu (K) concave core-shell tetrahedron and (L) individual irregularly shaped nanocrystal.

spacing was 0.14 nm. A periodic lattice is extended across the junction of Pd core (Fig. 5G) and PdPtRhIrRu shell (Fig. 5H). In addition, the bright and dark contrasts in the PdPtRhIrRu shell were observed again because of the different atomic weights. These observations are also similar to the HAADF-STEM images captured from a single Pd@PdPtRhIrRu concave core-shell octahedron (Fig. 5, I and J). The EDS analysis revealed that Pd elements are uniformly distributed throughout the tetrahedron (Fig. 5K), whereas Pt, Ir, Rh, and Ru elements are only located outside the tetrahedron. A similar result was also obtained when we characterized an individual irregularly shaped nanocrystal (Fig. 5L). These results suggest that the resultant nanocrystals indeed had a Pd-rich core with a solid-solution PdPtRhIrRu shell.

Figure 6 schematically illustrates how to manipulate the reduction kinetics and thus entropy of mixing to prepare the solid-solution HEA nanocrystals with different spatial compositions and surface atomic structures. As the control experiment, the one-pot synthesis could only induce the formation of the phase-separated PdPtRhIrRu nanocrystals due to the sequential reduction reactions of the different precursors. Compared to one-pot synthesis, the dropwise synthesis allows us to control the number of atoms generated from different types of precursors at the same value during the steady state, leading to the formation of PdPtRhIrRu nanocrystals with a typical solid-solution alloy phase. Along this line, by further shortening the duration of time between adjacent drops to increase the atom deposition rate greater than the surface diffusion rate, the dendritic solid-solution PdPtRhIrRu nanocrystals were obtained as the product. Furthermore, by influencing the redox potentials of metal precursor ions at low temperature and thus increasing gaps between the time to reach the steady state for the Pd and the other four Pt, Ir, Rh, and Ru precursors, the products became Pd@PdPtRhIrRu core-shell nanocrystals.

Electrocatalytic performance and mechanism

The electrocatalytic performances of solid-solution PdPtRhIrRu nanocrystals without/with a dendritic morphology toward both HER and HOR were investigated (Fig. 7 and figs. S16 to S22). In addition, the phase-separated PdPtRhIrRu nanocrystals and commercial Pt/C were measured for comparison. First, we evaluated their catalytic activities for HER in the acidic 0.5 M H_2SO_4 electrolyte. The linear sweep voltammogram (LSV) polarization curves of these four catalysts normalized by the electrode area (0.07 cm^2) were shown in Fig. 7A. The dendritic solid-solution PdPtRhIrRu nanocrystals exhibited the smallest overpotential of 30 mV (versus reversible hydrogen electrode, V_{RHE}) at a current density of 10 mA/cm^2 among these catalysts. Their geometric current densities, where the current is normalized by geometric electrode area, were calculated, as shown in Fig. 7B. The typical solid-solution PdPtRhIrRu HEA nanocrystals and the dendritic PdPtRhIrRu HEA nanocrystals showed geometric current densities of 21.2 and 26.8 mA/cm^2 at a potential of −0.05 V_{RHE}, which were 3.78 and 4.79 times higher than that of the phase-separated PdPtRhIrRu nanocrystals, respectively. This comparison suggested that the formation of the high-entropy solid-solution mixing that could induce the fine-tuning electronic structure of HEA nanocrystals and thus the synergistic effect (Fig. 4 and fig. S9) is the primary factor in enhancing the

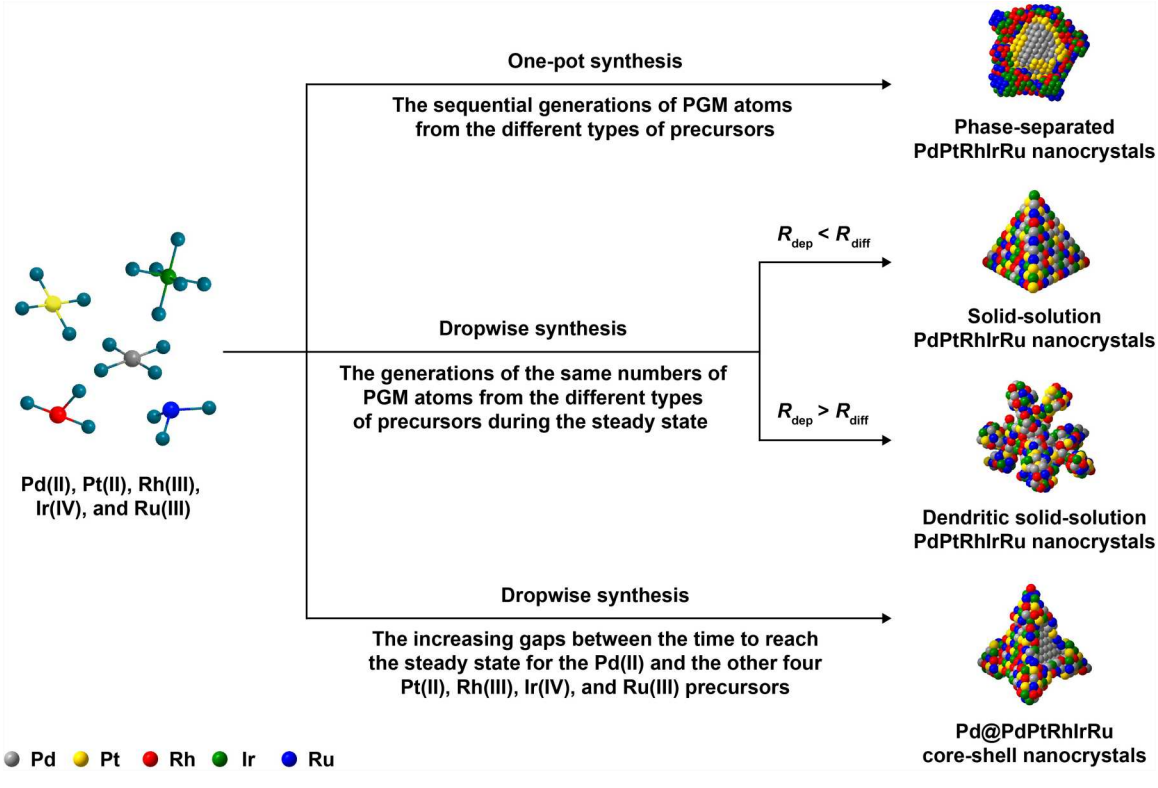

Fig. 6. Schematic illustrating how to manipulate the dropwise synthesis for the formation of solid-solution HEA nanocrystals with different spatial compositions and surface atomic structures.

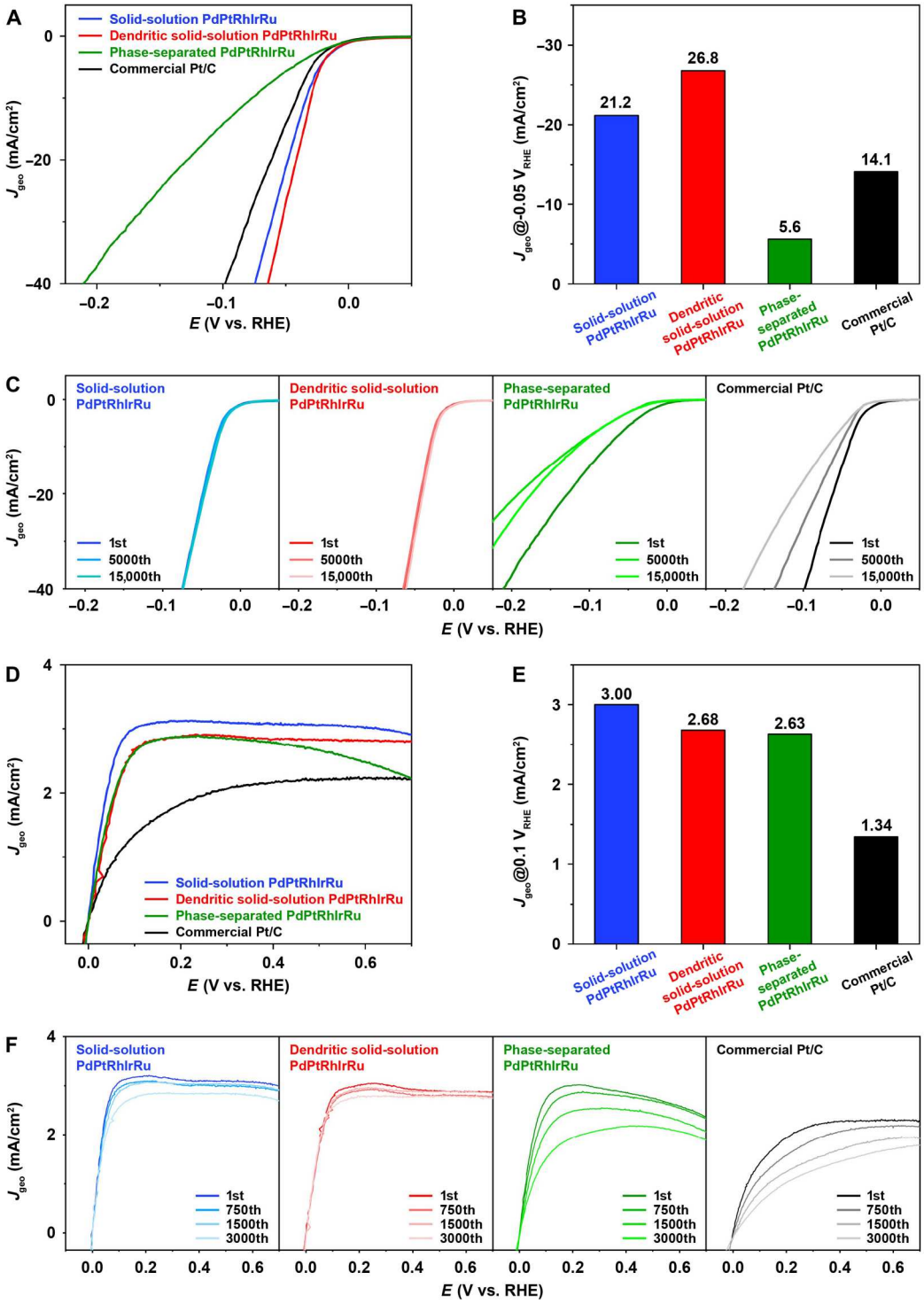

Fig. 7. Electrocatalytic activity and durability for HER and HOR. (**A** to **C**) HER performance. (A) LSV curves of solid-solution PdPtRhIrRu, dendritic solid-solution PdPtRhIrRu, phase-separated PdPtRhIrRu nanocrystals, and commercial Pt/C in 0.5 M H_2SO_4 solution. (B) Comparison of geometric current densities at an overpotential of 50 mV. (C) Comparison of the initial LSV curves for HER and the LSV curves after 5000, 10,000, and 15,000 cycles. (**D** to **F**) HOR performance. (D) LSV curves of solid-solution PdPtRhIrRu, dendritic solid-solution PdPtRhIrRu, phase-separated PdPtRhIrRu nanocrystals, and commercial Pt/C in H_2-saturated 0.1 M KOH solution. (E) Comparison of geometric current densities at an overpotential of 100 mV. (F) Comparison of the initial LSV curves for HOR and the LSV curves after 750, 1500, and 3000 cycles.

catalytic activity toward HER, while a high density of low-coordination surface atoms on the HEA nanocrystals could additionally promote the catalytic activity. Furthermore, the long-term durability tests were examined, as shown in Fig. 7C. Both PdPtRhIrRu HEA-based nanocrystals offered remarkable durability, showing negligible activity loss after 15,000 cycles of repeated catalytic measurements. They also exhibited good stability at a constant high current density of 100 mA/cm^2 (fig. S17). The morphologies of the HEA-based nanocrystals remained unaltered after the durability tests (fig. S18, A and B). In contrast, the phase-separated PdPtRhIrRu nanocrystals and commercial Pt/C lost 49.2% and 57.4% of their current densities at −0.05 V_{RHE} after 15,000 cycles, respectively. The outstanding durability could be attributed to the high-entropy stabilization effect in the HEA-based nanocrystals (*2*, *3*, *7*–*9*, *13*, *39*), also originating from the mixing of multiple elements (Figs. 2C, 3C, and 4 and fig. S9).

Second, we studied the catalytic activities of the catalysts for alkaline HOR, an important process for the hydrogen fuel cell. The HOR performances were examined by LSV polarization curves in N_2- and H_2-saturated 0.1 M KOH solution. As shown in fig. S19, a very small anodic current was observed in the N_2-saturated electrolyte. In contrast, the anodic current over 0 V_{RHE} was obtained upon H_2 saturation of the electrolyte, suggesting the H_2 oxidation, as shown in Fig. 7D. Compared to the commercial Pt/C sample, the solid-solution PdPtRhIrRu nanocrystals without/with dendritic morphology and phase-separated PdPtRhIrRu nanocrystals showed low HOR overpotentials within the full potential range. We also took the values of geometric current densities at a potential of 0.1 V_{RHE} and plotted them in Fig. 7E. The values of solid-solution PdPtRhIrRu nanocrystals without and with dendritic morphology and phase-separated PdPtRhIrRu nanocrystals (3.00, 2.68, and 2.63 mA/cm^2, respectively) were much larger than that of the commercial Pt/C (1.34 mA/cm^2). We then evaluated the long-term durability tests for the HOR. As shown in Fig. 7F, the solid-solution PdPtRhIrRu nanocrystals without and with a dendritic morphology still retained 85.0% (2.55 mA/cm^2) and 95.9% (2.57 mA/cm^2) geometric current densities at a potential of 0.1 V_{RHE} after 3000 cycles, respectively. Their morphologies remained intact with no obvious particle growth and agglomeration (fig. S18, C and D). In contrast, the polarization curves of the phase-separated PdPtRhIrRu nanocrystals and Pt/C samples showed obvious deterioration (Fig. 7F). Furthermore, the HEA-based nanocrystals exhibited much better catalytic performances than their quaternary solid-solution nanocrystals (i.e., PtRhIrRu, PdRhIrRu, PdPtIrRu, PdPtRhRu, and PdPtRhIr nanocrystals; figs. S20 to S22) for HER and HOR. Together, it is evident that the HEA-based nanocrystals not only showed remarkable initial activities toward HER and HOR but retained their activities to the largest extent during the accelerated durability tests.

We further used in situ XAS measurements to reveal the actual active sites and the synergistic effect among five elements of HEA nanocrystals during the catalysis. In the first set of in situ XAS experiments, we collected the XANES spectra at Pd K-edge, Pt L_3-edge, Rh K-edge, Ir L_3-edge, and Ru K-edge of the representative dendritic PdPtRhIrRu HEA nanocrystals under the open circuit potential (OCP) and different applied potentials (0.05 and −0.05 to −0.15 V_{RHE}) for HER in the acidic 0.5 M H_2SO_4 electrolyte (figs. S23 and S24). We observed that the absorption edge of Ru moved to lower energy when the applied potential was increased. The shift could be attributed to the increase of electron density and the adsorbed hydrogen ions on the Ru sites during HER (fig. S23) (*13*, *18*, *45*, *46*). By contrast, the absorption edges of the other four elements have almost no change with the increase in the applied potential. These observations suggested that Ru sites are the direct active sites for HER, and the other elements contribute to modifying the electronic structure and increasing the entropy of PdPtRhIrRu HEA nanocrystals (Fig. 4 and fig. S9). In addition, the EXAFS spectra of all five elements in the PdPtRhIrRu HEA nanocrystals with the increased applied potential revealed a negligible mismatch, indicating that the PdPtRhIrRu HEA nanocrystals maintained metallic states and exhibited extraordinary durability during HER (fig. S24) (*13*, *18*).

Furthermore, to clarify the effects of the low-coordination defect sites including step atoms (Fig. 3G), local disordered atoms (Fig. 3H), and vacancy defects (Fig. 3I) of the dendritic PdPtRhIrRu HEA nanocrystals on HER (Fig. 7, A to C), we have used the density functional theory (DFT) to calculate hydrogen-adsorption free energy (ΔG_{H^*}, which is widely used descriptor for the ability of HER) at the Ru active sites near these defect sites, as well as the defect-free sites (Fig. 8, figs. S25 to S27, and table S2) (*47*, *48*). On the basis of the calculated ΔG_{H^*} of HER for more than 100 possible atomic configurations of H-adsorbed PdPtRhIrRu surface, the Ru sites near the step sites have the smallest absolute ΔG_{H^*} among the four types of representative sites (Fig. 8). These statistical data suggest that the presence of the step sites around the Ru atoms could largely weaken the hydrogen adsorption on Ru and consequently promote the HER activity. Given the various configurations of multielement high-entropy mixing, further study along this line will advance our understanding of the surface-dependent catalytic activity of HEA nanocrystals.

In the second set of in situ XAS experiments for HOR in the H_2-saturated 0.1 M KOH solution (figs. S28 and S29), we also collected the XANES spectra at Pd K-edge, Pt L_3-edge, Rh K-edge, Ir L_3-edge, and Ru K-edge of the representative dendritic PdPtRhIrRu HEA nanocrystals under the OCP and different applied potentials (0.05 and 0.9 V_{RHE}). Our results indicate that the Pd sites play an important role in HOR, as evidenced by the dramatic shift in the main Pd K-edge toward lower energy when the applied potential was gradually changed from OCP, 0.05, to 0.9 V_{RHE} (fig. S28A). This shift could be attributed to the preadsorbed hydrogen atom (H_{ad}) reacting with the OH^- in the aqueous solution and/or the adsorbed OH_{ad} on the surface and, thus, the subsequent desorption of water molecules from the HEA surface (*49*–*51*). In addition, the very slight increase in the white line intensity of Ir L_3-edge suggests that the oxophilic nature of this element leads to the adsorption of OH_{ad}, which could further increase the rate of HOR (fig. S28D). By contrast, the absorption edges of the other three elements remained nearly unchanged at different potentials (fig. S28, B, C, and E). These observations suggest that the Pd atoms serve as the main active sites for HOR. Again, the EXAFS spectra of all five elements in the PdPtRhIrRu HEA nanocrystals showed a very minor mismatch during in situ XAS experiments, indicating that the PdPtRhIrRu HEA nanocrystals showed high durability for HOR (fig. S29) (*13*, *18*). Specifically, the catalytic performances of HEA catalysts were enhanced through the decoration of the active components on the HEA surfaces in recent studies (*52*, *53*). Further study to promote the interaction or synergistic effect between the multielement HEA support with a unique high-entropy

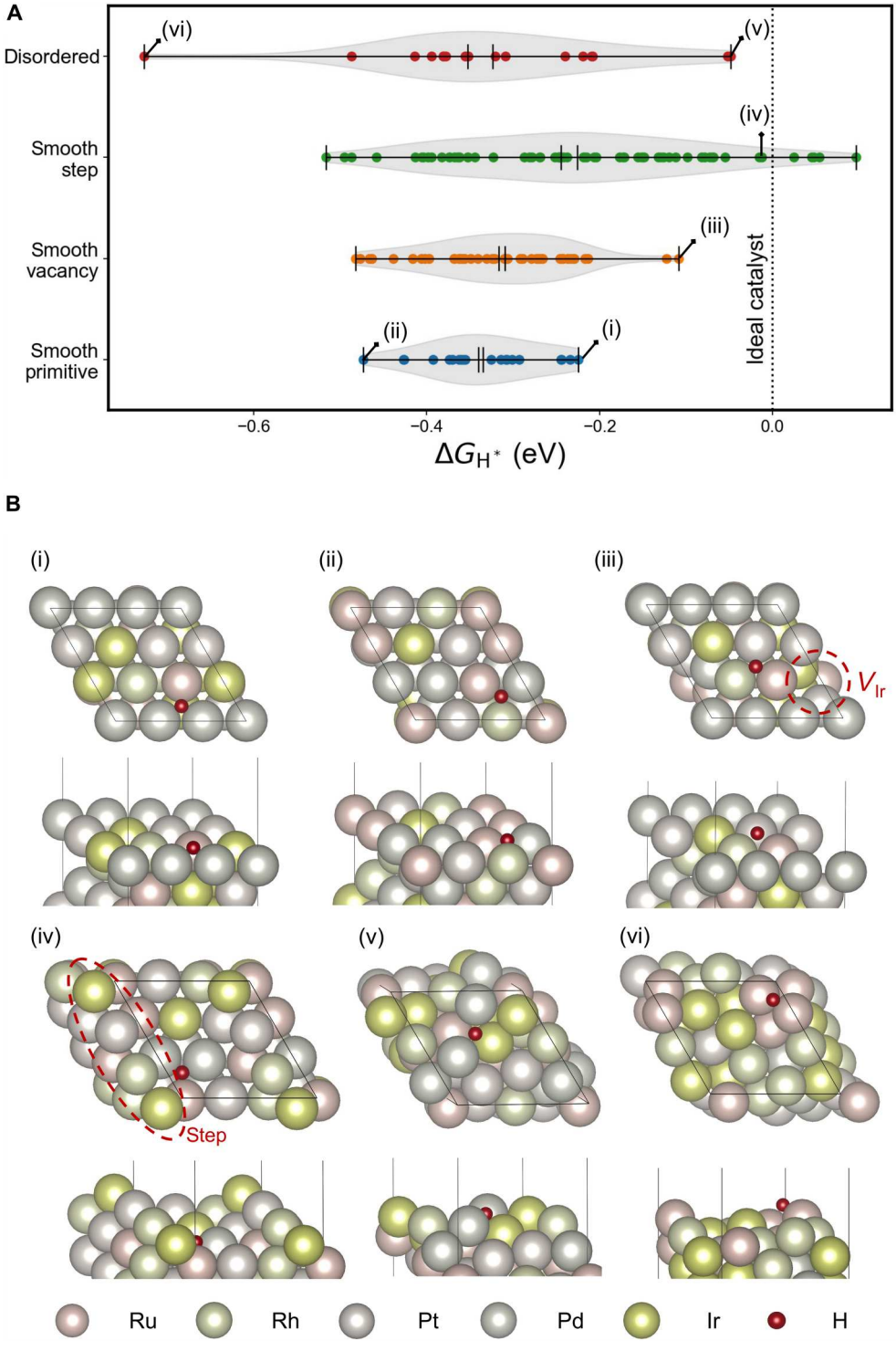

Fig. 8. Calculated hydrogen-adsorption free energy (ΔG_{H^*}) on HEA surface. (**A**) The violin plots of the calculated hydrogen-adsorption free energy for a variety of H adsorption configurations on the four different types of representative sites for PdPtRhIrRu HEA surfaces (smooth primitive, smooth vacancy, smooth step, and disordered atoms). (**B**) The representative structures of H-adsorbate indicated in (A) are illustrated (top and tilted side view).

coordination environment and the active component may greatly enhance the catalytic activity and thus high atomic efficiency (figs. S30 and S31).

DISCUSSION

We have quantitatively analyzed the reduction kinetics and entropy of mixing during the formation of solid-solution PdPtRhIrRu HEA nanocrystals with different spatial compositions and surface structures. On the basis of the quantitative data, we demonstrate that the dropwise synthesis can manipulate a steady state for the number of each metal precursor at the same and different periods during the synthesis. Therefore, three distinctive types of HEA nanocrystals including the typical solid-solution PdPtRhIrRu nanocrystals, dendritic solid-solution PdPtRhIrRu nanocrystals, and Pd@PdPtRhIrRu core-shell nanocrystals were obtained in a controllable and predictable manner. Compared to the commercial Pt/C and phase-separated PdPtRhIrRu nanocrystals, the dendritic solid-solution PdPtRhIrRu nanocrystals showed greatly enhanced activity and durability toward HER and HOR. Given the difficulty in deciphering the increased complexities in the multicomponent synthesis, this work will shed light on the synthesis of HEA nanocrystals and their derivatives for catalysis. The mechanistic insights obtained in this work can be extended to other systems involving HEA nanocrystals made of commonly used catalytically active Au, Ag, Cu, Fe, Co, Ni, Mo, or W as mixed elements.

MATERIALS AND METHODS

Materials

Sodium tetrachloropalladate(II) (Na_2PdCl_4), potassium tetrachloroplatinate(II) (K_2PtCl_4), rhodium(III) chloride hydrate ($RhCl_3{\cdot}xH_2O$), hydrogen hexachloroiridate(IV) chloride hydrate ($H_2IrCl_6{\cdot}xH_2O$), ruthenium(III) chloride hydrate ($RuCl_3{\cdot}xH_2O$), AA, potassium bromide (KBr), and PVP (weight-average molecular weight ≈ 55,000), aqueous hydrochloric acid (HCl; 37% by weight), aqueous nitric acid (HNO_3; 70% by weight), and EG were all obtained from Sigma-Aldrich. Deionized (DI) water with a resistivity of 18.2 megohm·cm was used for all the experiments.

Quantitative analysis of the reduction kinetics of Pd(II), Pt(II), Rh(III), Ir(IV), and Ru(III) precursors using ICP-OES

The reduction kinetics of the Pd(II), Pt(II), Rh(III), Ir(IV), and Ru(III) precursors were measured by analyzing the amounts of atoms in the reaction solutions at different time points through the ICP-OES measurements (*28*). In a typical experiment, 7 ml of EG solution containing PVP (50 mg), AA (50 mg), and KBr (0 or 75 mg) were added into a 20-ml vial and subsequently preheated at a specific temperature (140° or 180°C) in an oil bath under magnetic stirring for 5 min. Then, 3 ml of EG solution containing Na_2PdCl_4 (9.71 mg), K_2PtCl_4 (13.7 mg), $RhCl_3{\cdot}xH_2O$ (8.69 mg), $H_2IrCl_6{\cdot}xH_2O$ (15.21 mg), and $RuCl_3{\cdot}xH_2O$ (8.63 mg) at an equal molar amount was injected into the reaction solution using a pipette. Meanwhile, the timer started running. and 0.1 ml of aliquots were taken from the sample at the specific time points and immediately transferred to 0.9 ml of DI water held in an ice bath to quench the reduction of metal precursors. Afterward, aliquots were centrifuged at 30,000 rpm for 30 min to precipitate out all the solid nanoparticles, leaving the remaining metal ions in the supernatant. Last, the solid products were dissolved in an aqua regia solution for 24 hours and further diluted with 1% (v/v) aqueous HNO_3 solution for the ICP-OES analysis.

Calculations of the instantaneous percentages of Pd, Pt, Rh, Ir, and Ru atoms, the instantaneous entropy of mixing, and the percentages of Pd, Pt, Rh, Ir, and Ru elements in the product as a function of reaction time

The number of metal precursor ions (n_t) remaining in the reaction solution at reaction time t could be derived using Eq. 2. By using Eq. 2, we are able to quantitatively account for the numbers of the metal atoms generated from the reduction reactions of metal precursors between each adjacent drop $[n_0 - (n_t - n_{t-\tau})]$ as a function of time, which could be further used to calculate the instantaneous percentages of Pd, Pt, Rh, Ir, and Ru atoms during the synthesis. In addition, on the basis of these quantitative data, the instantaneous entropy of mixing as a function of time also could be determined using Eq. 1. Furthermore, we could estimate the number of metal atoms generated $[(n_0 \times N_t) - (n_t)]$ for each precursor at each time point t, where N_t represents the total number of droplets added up to time t. We could further add up the total metal atoms generated up to time t of the five elements and calculate their total percentages in the product as a function of reaction time.

One-pot synthesis of phase-separated multimetallic nanocrystals

Seven milliliters of EG solution containing PVP (50 mg) and AA (50 mg) was added into a 250-ml long-neck round-bottom flask and subsequently preheated at 180°C in an oil bath under magnetic stirring for 5 min. Then, 3 ml of EG solution including Na_2PdCl_4 (9.71 mg), K_2PtCl_4 (13.7 mg), $RhCl_3{\cdot}xH_2O$ (8.69 mg), $H_2IrCl_6{\cdot}xH_2O$ (15.21 mg), and $RuCl_3{\cdot}xH_2O$ (8.63 mg) at an equal molar amount was injected into the reaction solution in one shot using a pipette. The vial was then capped and maintained at 180°C under magnetic stirring for 10 hours. After the reaction, the PdPtRhIrRu phase-separated nanocrystals were collected by centrifugation, washed once with acetone and three times with water, and lastly dispersed in water for further use.

Dropwise synthesis of solid-solution HEA nanocrystals

In a typical synthesis, 7 ml of EG solution containing PVP (50 mg) and AA (50 mg) was added into a 250-ml long-neck round-bottom flask and subsequently preheated at 180°C in an oil bath under magnetic stirring for 5 min. Then, 3 ml of EG solution containing Na_2PdCl_4 (9.71 mg), K_2PtCl_4 (13.7 mg), $RhCl_3{\cdot}xH_2O$ (8.69 mg), $H_2IrCl_6{\cdot}xH_2O$ (15.21 mg), and $RuCl_3{\cdot}xH_2O$ (8.63 mg) at an equal molar amount was introduced dropwise into the reaction solution by a syringe pump at a specific rate of 0.5 ml/hour (τ = 68.4 s). After the reaction, the PdPtRhIrRu HEA nanocrystals were collected by centrifugation, washed once with acetone and three times with water, and lastly dispersed in water for further use. Note that the PdPtRhIrRu HEA nanocrystals with different compositions (such as the Pd-rich and Pt-rich PdPtRhIrRu HEA nanocrystals) could also be controlled by adjusting the ratios of metal precursors added into the synthesis under the standard procedures.

Dropwise synthesis of dendritic solid-solution HEA nanocrystals

In a typical synthesis, 7 ml of EG solution containing PVP (50 mg) and AA (50 mg) was added into a 250-ml long-neck round-bottom flask and subsequently preheated at 180°C in an oil bath under magnetic stirring for 5 min. Then, 3 ml of EG solution including Na_2PdCl_4 (9.71 mg), K_2PtCl_4 (13.7 mg), $RhCl_3{\cdot}xH_2O$ (8.69 mg), $H_2IrCl_6{\cdot}xH_2O$ (15.21 mg), and $RuCl_3{\cdot}xH_2O$ (8.63 mg) at an equal molar amount was introduced dropwise into the reaction solution by a syringe pump at a specific rate of 3 ml/hour (τ = 11.4 s). After the reaction, the dendritic PdPtRhIrRu HEA nanocrystals were collected by centrifugation, washed once with acetone and three times with water, and lastly dispersed in water for further use. Note that the quaternary solid-solution nanocrystals with different compositions (PtRhIrRu, PdRhIrRu, PdPtIrRu, PdPtRhRu, and PdPtRhIr nanocrystals) were prepared using the similar standard procedures described above except for changing the combination of the precursors.

Dropwise synthesis of Pd@HEA core-shell nanocrystals

In a typical synthesis, 7 ml of EG solution containing PVP (50 mg), AA (50 mg), and KBr (75 mg) was added into a 250-ml long-neck round-bottom flask and subsequently preheated at 140°C in an oil bath under magnetic stirring for 5 min. Then, 3 ml of EG solution including Na_2PdCl_4 (9.71 mg), K_2PtCl_4 (13.7 mg), $RhCl_3{\cdot}xH_2O$ (8.69 mg), $H_2IrCl_6{\cdot}xH_2O$ (15.21 mg), and $RuCl_3{\cdot}xH_2O$ (8.63 mg) at an equal molar amount was introduced dropwise into the reaction solution by a syringe pump at a specific rate of 0.125 ml/hour (τ = 273.5 s). After the reaction, the Pd@PdPtRhIrRu core-shell nanocrystals were collected by centrifugation, washed once with acetone and three times with water, and lastly dispersed in water for further use.

Seed-mediated growth of hybrid HEA-Ru and HEA-Pd nanocrystals

In a standard seed-mediated growth for the synthesis of hybrid HEA-Ru nanocrystals, 1.0 ml of the suspension of the dendritic solid-solution PdPtRhIrRu HEA nanocrystals in EG, 20 mg of AA, 100 mg of PVP, 60 mg of KBr, and 2.5 ml of EG were added into a 20-ml vial. Under magnetic stirring, the reaction solution was heated at 110°C for 20 min and raised to 195°C within 20 min under magnetic stirring. Then, 7 ml of $RuCl_3{\cdot}3H_2O$ precursor solution (2.75×10^{-2} and 5.5×10^{-2} mg/ml) in EG was titrated into the reaction solution at a rate of 0.8 ml/hour by a syringe pump at 195°C, to obtain the hybrid HEA-Ru nanocrystals with the Ru loadings of 5 and 10 atomic % (at %), respectively. The reaction was kept at 195°C for an additional 1 hour after the precursor solution was introduced. After the reaction, the hybrid HEA-Ru nanocrystals with Ru exposed on the surface of HEA nanocrystals were collected by centrifugation, washed once with acetone and three times with water, and lastly dispersed in water for further use. The procedures for the synthesis of hybrid HEA-Pd nanocrystals with the Pd loadings of 5 and 10 at % are similar to the standard seed-mediated growth described above except for changing the precursor to Na_2PdCl_4.

Electrocatalytic measurements for HER

In a standard procedure for the preparation of catalyst samples, 1.5 mg of the nanocrystals and 6 mg of carbon support (Vulcan XC-72R) were dispersed in 3 and 12 ml of water, respectively, and then evenly mixed by ultrasonication at room temperature for 3 hours. Then, the carbon-supported nanocrystals were collected by centrifugation and further treated in 10 ml of acetic acid at 60°C for 3 hours to make their surface clean. After being washed four times with ethanol and four times with water, the sample was dried at 60°C for 2 hours and 90°C for 1 hour in an oven. For the preparation of the catalyst ink, a solution containing 0.5 ml of isopropanol, 0.5 ml of water, and 20 μl of 5% Nafion was used to uniformly disperse 1 mg of the dried sample under ultrasonication for 15 min. Then, 3.6 μl of the suspension was loaded onto a polished glassy carbon rotating disk electrode with a geometric surface area of 0.07 cm^2 and subsequently dried under an isopropanol-saturated atmosphere at room temperature overnight. On the basis of the result of ICP-OES, the loading amount of metals was 20 weight %.

We conducted the HER measurements in a three-electrode system using a PGSTAT204 (Metrohm Autolab) electrochemical workstation. N_2-saturated 0.5 M H_2SO_4 (pH 0.2) was used as the electrolyte, and glassy carbon, Pt, and Ag/AgCl were used as the working electrode, counter electrode, and reference electrode, respectively. In a typical HER measurement, the electrode was subjected to 150 cycles of cyclic voltammetry (CV) with a high scan rate of 500 mV/s to obtain a stable surface. Then we applied −0.02 V (versus RHE) for 2 minutes to eliminate surface oxides. After the pretreatments, we recorded 5 cycles of CVs at a scan rate of 50 mV/s and made sure that they overlapped in the range of 0.05–1.1 V (versus RHE). We conducted the linear sweep voltammetry (LSV) from 0.1 to −0.25 V (versus RHE) at a scan rate of 1 mV/s and a rotating speed of 1600 rpm/s to evaluate the HER performance. For the long-term stability test, we carried out 15,000 cycles of CV in the same region as LSV for HER at 50 mV/s. All electrochemical measurements were conducted at room temperature and repeated three times to ensure reproducibility with iR compensation. The measured potentials versus Ag/AgCl were standardized with RHE on the basis of E versus RHE = $E_{measured}$ + 0.059 pH + 0.199.

Electrocatalytic measurements for HOR

The procedure for the preparation of catalyst samples and the three-electrode electrochemical system were the same as those used for HER measurements. For the HOR measurements, an Hg/HgO electrode was served as the reference electrode, and 0.1 M KOH was used as the electrolyte. The electrolyte was first purged with N_2 gas for 30 min before the electrocatalytic measurement. The electrode surface was cleaned by 50 cycles of CV test with the potential range from 0.05 to 1.05 V (versus RHE) at a high scan rate of 500 mV/s. We then performed the catalytic measurement in the 0.1 M KOH solution purged with N_2 and H_2 gases, respectively. The CV and LSV curves were recorded from −0.05 V to 0.7 V (versus RHE) under a rotating speed of 1600 rpm and a scan rate of 10 and 5 mV/s, respectively. For the long-term durability test, we carried out 3000 cycles of CV in the same region at a scan rate of 500 mV/s in the H_2-saturated electrolyte. The measured potentials versus Hg/HgO were standardized with an RHE on the basis of E versus RHE = $E_{measured}$ + 0.059 pH + 0.118.

DFT calculation

All computations were performed using DFT with the Perdew-Burke-Ernzerhof functional (*54*, *55*), as implemented in the Vienna Ab initio Simulation Package (*56*). The valence electron

wave functions were expanded in plane-wave basis sets with a 400-eV cutoff, and the projector augmented wave method was used to describe the core-electron interactions (*57*). A $6 \times 6 \times 1$ *k*-point grid was sampled using the Monkhorst-Pack scheme for each computation. All structures were fully optimized until the residual forces on the constituent atoms became less than 0.02 eV/Å, while keeping the lattice parameter fixed, which was taken from the experiment. For molecular dynamics part, we performed NVT simulations using Nose-Hoover thermostat with SMASS = 1.0 and a 1.0-fs integration time step. For further computational details, please refer to the "Computational details" section in the Supplementary Materials.

Characterizations

We analyzed the element contents using an iCAP 7200 ICP-OES (Thermo Fisher Scientific). We obtained TEM and HAADF-STEM images and EDS mapping on a spherical aberration–corrected field-emission TEM (JEOL, JEM-ARM200FTH) operated at 200 kV. We studied the crystal structures using XRD on an x-ray diffractometer (Bruker, D8). We analyzed the surface chemistry through XPS with a high-resolution x-ray photoelectron spectrometer (ULVAC-PHI, PHI Quantera II). The ex situ and in situ XAS spectra were recorded at beamline TPS 44A of the National Synchrotron Radiation Research Center.

Supplementary Materials

This PDF file includes:

Figs. S1 to S31

Tables S1 and S2

REFERENCES AND NOTES

1. J.-W. Yeh, S.-K. Chen, S.-J. Lin, J.-Y. Gan, T.-S. Chin, T.-T. Shun, C.-H. Tsau, S.-Y. Chang, Nanostructured high-entropy alloys with multiple principal elements: Novel alloy design concepts and outcomes. *Adv. Eng. Mater.* **6**, 299–303 (2004).
2. E. P. George, D. Raabe, R. O. Ritchie, High-entropy alloys. *Nat. Rev. Mater.* **4**, 515–534 (2019).
3. Q. Ding, Y. Zhang, X. Chen, X. Fu, D. Chen, S. Chen, L. Gu, F. Wei, H. Bei, Y. Gao, M. Wen, J. Li, Z. Zhang, T. Zhu, R. O. Ritchie, Q. Yu, Tuning element distribution, structure and properties by composition in high-entropy alloys. *Nature* **574**, 223–227 (2019).
4. Z. Rao, P.-Y. Tung, R. Xie, Y. Wei, H. Zhang, A. Ferrari, T. P. C. Klaver, F. Kormann, P. T. Sukumar, A. K. d. Silva, Y. Chen, Z. Li, D. Ponge, J. Neugebauer, O. Gutfleisch, S. Bauer, D. Raabe, Machine learning-enabled high-entropy alloy discovery. *Science* **378**, 78–85 (2022).
5. J. Yan, S. Yin, M. Asta, R. O. Ritchie, J. Ding, Q. Yu, Anomalous size effect on yield strength enabled by compositional heterogeneity in high-entropy alloy nanoparticles. *Nat. Commun.* **13**, 2789 (2022).
6. J. Ren, Y. Zhang, D. Zhao, Y. Chen, S. Guan, Y. Liu, L. Liu, S. Peng, F. Kong, J. D. Poplawsky, G. Gao, T. Voisin, K. An, Y. M. Wang, K. Y. Xie, T. Zhu, W. Chen, Strong yet ductile nanolamellar high-entropy alloys by additive manufacturing. *Nature* **608**, 62–68 (2022).
7. Y. Sun, S. Dai, High-entropy materials for catalysis: A new frontier. *Sci. Adv.* **7**, eabg1600 (2021).
8. Y. Yao, Q. Dong, A. Brozena, J. Luo, J. Miao, M. Chi, C. Wang, I. G. Kevrekidis, Z. J. Ren, J. Greeley, G. Wang, A. Anapolsky, L. Hu, High-entropy nanoparticles: Synthesis-structure-property relationships and data-driven discovery. *Science* **376**, eabn3103 (2022).
9. Y. Yao, Z. Huang, P. Xie, S. D. Lacey, R. J. Jacob, H. Xie, F. Chen, A. Nie, T. Pu, M. Rehwoldt, D. Yu, M. R. Zachariah, C. Wang, R. Shahbazian-Yassar, J. Li, L. Hu, Carbothermal shock synthesis of high-entropy-alloy nanoparticles. *Science* **359**, 1489–1494 (2018).
10. P. Xie, Y. Yao, Z. Huang, Z. Liu, J. Zhang, T. Li, G. Wang, R. Shahbazian-Yassar, L. Hu, C. Wang, Highly efficient decomposition of ammonia using high-entropy alloy catalysts. *Nat. Commun.* **10**, 4011 (2019).
11. D. Wu, K. Kusada, T. Yamamoto, T. Toriyama, S. Matsumura, S. Kawaguchi, Y. Kubota, H. Kitagawa, Platinum-group-metal high-entropy-alloy nanoparticles. *J. Am. Chem. Soc.* **142**, 13833–13838 (2020).
12. H. Li, Y. Han, H. Zhao, W. Qi, D. Zhang, Y. Yu, W. Cai, S. Li, J. Lai, B. Huang, L. Wang, Fast site-to-site electron transfer of high-entropy alloy nanocatalyst driving redox electrocatalysis. *Nat. Commun.* **11**, 5437 (2020).
13. G. Feng, F. Ning, J. Song, H. Shang, K. Zhang, Z. Ding, P. Gao, W. Chu, D. Xia, Sub-2 nm ultrasmall high-entropy alloy nanoparticles for extremely superior electrocatalytic hydrogen evolution. *J. Am. Chem. Soc.* **143**, 17117–17127 (2021).
14. K. Mori, N. Hashimoto, N. Kamiuchi, H. Yoshida, H. Kobayashi, H. Yamashita, Hydrogen spillover-driven synthesis of high-entropy alloy nanoparticles as a robust catalyst for CO_2 hydrogenation. *Nat. Commun.* **12**, 3884 (2021).
15. C. Zhan, Y. Xu, L. Bu, H. Zhu, Y. Feng, T. Yang, Y. Zhang, Z. Yang, B. Huang, Q. Shao, X. Huang, Subnanometer high-entropy alloy nanowires enable remarkable hydrogen oxidation catalysis. *Nat. Commun.* **12**, 6261 (2021).
16. T. Li, Y. Yao, Z. Huang, P. Xie, Z. Liu, M. Yang, J. Gao, K. Zeng, A. Brozena, G. Pastel, M. Jiao, Q. Dong, J. Dai, S. Li, H. Zong, M. Chi, J. Luo, Y. Mo, G. Wang, C. Wang, R. Shahbazian-Yassar, L. Hu, Denary oxide nanoparticles as highly stable catalysts for methane combustion. *Nat. Catal.* **4**, 62–70 (2021).
17. L. Tao, M. Sun, Y. Zhou, M. Luo, F. Lv, M. Li, Q. Zhang, L. Gu, B. Huang, S. Guo, A general synthetic method for high-entropy alloy subnanometer ribbons. *J. Am. Chem. Soc.* **144**, 10582–10590 (2022).
18. J. Hao, Z. Zhuang, K. Cao, G. Gao, C. Wang, F. Lai, S. Lu, P. Ma, W. Dong, T. Liu, M. Du, H. Zhu, Unraveling the electronegativity-dominated intermediate adsorption on high-entropy alloy electrocatalysts. *Nat. Commun.* **13**, 2662 (2022).
19. B. Wang, C. Wang, X. Yu, Y. Cao, L. Gao, C. Wu, Y. Yao, Z. Lin, Z. Zou, General synthesis of high-entropy alloy and ceramic nanoparticles in nanoseconds. *Nat. Synth.* **1**, 138–146 (2022).
20. C.-L. Yang, L.-N. Wang, P. Yin, J. Liu, M.-X. Chen, Q.-Q. Yan, Z.-S. Wang, S.-L. Xu, S.-Q. Chu, C. Cui, H. Ju, J. Zhu, Y. Lin, J. Shui, H.-W. Liang, Sulfur-anchoring synthesis of platinum intermetallic nanoparticle catalysts for fuel cells. *Science* **374**, 459–464 (2021).
21. M. Cui, C. Yang, S. Hwang, M. Yang, S. Overa, Q. Dong, Y. Yao, A. H. Brozena, D. A. Cullen, M. Chi, T. F. Blum, D. Morris, Z. Finfrock, X. Wang, P. Zhang, V. G. Goncharov, X. Guo, J. Luo, Y. Mo, F. Jiao, L. Hu, Multi-principal elemental intermetallic nanoparticles synthesized via a disorder-to-order transition. *Sci. Adv.* **8**, eabm4322 (2022).
22. H. Minamihara, K. Kusada, D. Wu, T. Yamamoto, T. Toriyama, S. Matsumura, L. S. R. Kumara, K. Ohara, O. Sakata, S. Kawaguchi, Y. Kubota, H. Kitagawa, Continuous-flow reactor synthesis for homogeneous 1 nm-sized extremely small high-entropy alloy nanoparticles. *J. Am. Chem. Soc.* **144**, 11525–11529 (2022).
23. D. Wu, K. Kusada, Y. Nanba, M. Koyama, T. Yamamoto, T. Toriyama, S. Matsumura, O. Seo, I. Gueye, J. Kim, L. S. R. Kumara, O. Sakata, S. Kawaguchi, Y. Kubota, H. Kitagawa, Noble-metal high-entropy-alloy nanoparticles: Atomic-level insight into the electronic structure. *J. Am. Chem. Soc.* **144**, 3365–3369 (2022).
24. K. D. Gilroy, A. Ruditskiy, H.-C. Peng, D. Qin, Y. Xia, Bimetallic nanocrystals: Syntheses, properties, and applications. *Chem. Rev.* **116**, 10414–10472 (2016).
25. P.-C. Chen, X. Liu, J. L. Hedrick, Z. Xie, S. Wang, Q.-Y. Lin, M. C. Hersam, V. P. Dravid, C. A. Mirkin, Polyelemental nanoparticle libraries. *Science* **352**, 1565–1569 (2016).
26. P.-C. Chen, M. Liu, J. S. Du, B. Meches, S. Wang, H. Lin, V. P. Dravid, C. Wolverton, C. A. Mirkin, Interface and heterostructure design in polyelemental nanoparticles. *Science* **363**, 959–964 (2019).
27. B. Shen, L. Huang, J. Shen, K. He, C. Y. Zheng, V. P. Dravid, C. Wolverton, C. A. Mirkin, Crystal structure engineering in multimetallic high-index facet nanocatalysts. *Proc. Natl. Acad. Sci. U.S.A.* **118**, e2105722118 (2021).
28. M. Zhou, H. Wang, M. Vara, Z. D. Hood, M. Luo, T.-H. Yang, S. Bao, M. Chi, P. Xiao, Y. Zhang, Y. Xia, Quantitative analysis of the reduction kinetics responsible for the one-pot synthesis of Pd-Pt bimetallic nanocrystals with different structures. *J. Am. Chem. Soc.* **138**, 12263–12270 (2016).
29. Q. Zhang, K. Kusada, D. Wu, T. Yamamoto, T. Toriyama, S. Matsumura, S. Kawaguchi, Y. Kubota, H. Kitagawa, Crystal structure control of binary and ternary solid-solution alloy nanoparticles with a face-centered cubic or hexagonal close-packed phase. *J. Am. Chem. Soc.* **144**, 4224–4232 (2022).
30. Y. Shi, Z. Lyu, M. Zhao, R. Chen, Q. N. Nguyen, Y. Xia, Noble-metal nanocrystals with controlled shapes for catalytic and electrocatalytic applications. *Chem. Rev.* **121**, 649–735 (2021).
31. T.-H. Yang, K. D. Gilroy, Y. Xia, Reduction rate as a quantitative knob for achieving deterministic synthesis of colloidal metal nanocrystals. *Chem. Sci.* **8**, 6730–6749 (2017).
32. H.-C. Peng, J. Park, L. Zhang, Y. Xia, Toward a quantitative understanding of symmetry reduction involved in the seed-mediated growth of Pd nanocrystals. *J. Am. Chem. Soc.* **137**, 6643–6652 (2015).
33. T.-H. Yang, H.-C. Peng, S. Zhou, C.-T. Lee, S. Bao, Y.-H. Lee, J.-M. Wu, Y. Xia, Toward a quantitative understanding of the reduction pathways of a salt precursor in the synthesis of metal nanocrystals. *Nano Lett.* **17**, 334–340 (2017).

34. T.-H. Yang, S. Zhou, K. D. Gilroy, L. Figueroa-Cosme, Y.-H. Lee, J.-M. Wu, Y. Xia, Autocatalytic surface reduction and its role in controlling seed-mediated growth of colloidal metal nanocrystals. *Proc. Natl. Acad. Sci. U.S.A.* **114**, 13619–13624 (2017).
35. Q. Zhang, K. Kusada, D. Wu, T. Yamamoto, T. Toriyama, S. Matsumura, S. Kawaguchi, Y. Kubota, H. Kitagawa, Selective control of fcc and hcp crystal structures in Au-Ru solid-solution alloy nanoparticles. *Nat. Commun.* **9**, 510 (2018).
36. F. Gao, Y. Zhang, Z. Wu, H. You, Y. Du, Universal strategies to multi-dimensional noble-metal-based catalysts for electrocatalysis. *Coord. Chem. Rev.* **436**, 213825 (2021).
37. Y. Zhang, F. Gao, H. You, Z. Li, B. Zou, Y. Du, Recent advances in one-dimensional noble-metal-based catalysts with multiple structures for efficient fuel-cell electrocatalysis. *Coord. Chem. Rev.* **450**, 214244 (2022).
38. Y. Zhang, F. Gao, D. Wang, Z. Li, X. Wang, C. Wang, K. Zhang, Y. Du, Amorphous/crystalline heterostructure transition-metal-based catalysts for high-performance water splitting. *Coord. Chem. Rev.* **475**, 214916 (2023).
39. J.-W. Yeh, Alloy design strategies and future trends in high-entropy alloys. *JOM* **65**, 1759–1771 (2013).
40. J. F. Modulder, W. F. Stickle, P. E. Sobol, K. D. Bomben, *Handbook of X-ray Photoelectron Spectroscopy* (Perkin-Elmer, 1992).
41. B. Lim, M. Jiang, P. H. C. Camargo, E. C. Cho, J. Tao, X. Lu, Y. Zhu, Y. Xia, Pd-Pt bimetallic nanodendrites with high activity for oxygen reduction. *Science* **324**, 1302–1305 (2009).
42. L. Bu, S. Guo, X. Zhang, X. Shen, D. Su, G. Lu, X. Zhu, J. Yao, J. Guo, X. Huang, Surface engineering of hierarchical platinum-cobalt nanowires for efficient electrocatalysis. *Nat. Commun.* **7**, 11850 (2016).
43. C. Li, Q. Yuan, B. Ni, T. He, S. Zhang, Y. Long, L. Gu, X. Wang, Dendritic defect-rich palladium-copper-cobalt nanoalloys as robust multifunctional non-platinum electrocatalysts for fuel cells. *Nat. Commun.* **9**, 3702 (2018).
44. K. D. Gilroy, X. Yang, S. Xie, M. Zhao, D. Qin, Y. Xia, Shape-controlled synthesis of colloidal metal nanocrystals by replicating the surface atomic structure on the seed. *Adv. Mater.* **30**, 1706312 (2018).
45. D. Morris, Y. Yao, Y. Z. Finfrock, Z. Huang, R. Shahbazian-Yassar, L. Hu, P. Zhang, Composition-dependent structure and properties of 5- and 15-element high-entropy alloy nanoparticles. *Cell Rep. Phys. Sci.* **2**, 100641 (2021).
46. H. Asakura, K. Teramura, T. Shishido, T. Tanaka, N. Yan, C. Xiao, S. Yao, Y. Kou, *In situ* time-resolved DXAFS study of Rh nanoparticle formation mechanism in ethylene glycol at elevated temperature. *Phys. Chem. Chem. Phys.* **14**, 2983–2990 (2012).
47. J. K. Nørskov, T. Bligaard, A. Logadottir, J. R. Kitchin, J. G. Chen, S. Pandelov, U. Stimming, Trends in the exchange current for hydrogen evolution. *J. Electrochem. Soc.* **152**, J23 (2005).
48. J. Greeley, T. Jaramillo, J. Bonde, I. Chorkendorff, J. K. Nørskov, Computational high-throughput screening of electrocatalytic materials for hydrogen evolution. *Nat. Mater.* **5**, 909–913 (2006).
49. D. Strmcnik, M. Uchimura, C. Wang, R. Subbaraman, N. Danilovic, D. v. d. Vliet, A. P. Paulikas, V. R. Stamenkovic, N. M. Markovic, Improving the hydrogen oxidation reaction rate by promotion of hydroxyl adsorption. *Nat. Chem.* **5**, 300–306 (2013).
50. L. Han, P. Ou, W. Liu, X. Wang, H.-T. Wang, R. Zhang, C.-W. Pao, X. Liu, W.-F. Pong, J. Song, Z. Zhuang, M. V. Mirkin, J. Luo, H. L. Xin, Design of Ru-Ni diatomic sites for efficient alkaline hydrogen oxidation. *Sci. Adv.* **8**, eabm3779 (2022).
51. J. Hu, K. A. Kuttiyiel, K. Sasaki, C. Zhang, R. R. Adzic, Determination of hydrogen oxidation reaction mechanism based on Pt–H_{ad} energetics in alkaline electrolyte. *J. Electrochem. Soc.* **165**, J3355–J3362 (2018).
52. K. Zeng, J. Zhang, W. Gao, L. Wu, H. Liu, J. Gao, Z. Li, J. Zhou, T. Li, Z. Liang, B. Xu, Y. Yao, Surface-decorated high-entropy alloy catalysts with significantly boosted activity and stability. *Adv. Funct. Mater.* **32**, 2204643 (2022).
53. W. Shi, H. Liu, Z. Li, C. Li, J. Zhou, Y. Yuan, F. Jiang, K. Fu, Y. Yao, High-entropy alloy stabilized and activated Pt clusters for highly efficient electrocatalysis. *SusMat* **2**, 186–196 (2022).
54. J. P. Perdew, K. Burke, M. Ernzerhof, Generalized gradient approximation made simple. *Phys. Rev. Lett.* **77**, 3865–3868 (1996).
55. J. P. Perdew, K. Burke, M. Ernzerhof, Generalized gradient approximation made simple. *Phys. Rev. Lett.* **78**, 1396 (1997).
56. G. Kresse, J. Furthmüller, Efficient iterative schemes for ab initio total-energy calculations using a plane-wave basis set. *Phys. Rev. B Condens Matter.* **54**, 11169–11186 (1996).
57. G. Kresse, D. Joubert, From ultrasoft pseudopotentials to the projector augmented-wave method. *Phys. Rev. B* **59**, 1758–1775 (1999).

Acknowledgments: We thank National Center for High-performance Computing (NCHC) for providing computational and storage resources. **Funding:** We acknowledge the financial support by the Ministry of Science and Technology of Taiwan through the grants of MOST 110-2636-E-007-024. **Author contributions:** T.-H.Y. conceived and supervised the research. T.-H.Y., Y.-H.L., and C.-J.H. performed most of the experiments and data analysis. Y.-C.H., C.-W.C., S.-C.L., and J.-Q.G. prepared the electrodes and helped with electrochemical measurements. C.-C.C., J.-T.L., Y.-M.C., M.-Y.L., and S.Z. conducted HAADF-STEM micrographs and mapping images. L.-C.H., C.-Y.W., and C.-W.P. conducted the synchrotron XAS experiments. K.-H.L. carried out the DFT calculations. The manuscript was written through the discussion by all authors. All authors have approved the final version of manuscript. **Competing interests:** The authors declare that they have no competing interests. **Data and materials availability:** All data needed to evaluate the conclusions in the paper are present in the paper and/or the Supplementary Materials: kinetics analysis, TEM and HAADF-STEM images, EDS analysis, XRD analysis, electrochemistry, XAS analysis, and DFT computations. In addition, the structures and ΔG_{H^*} of various slabs considered in the DFT computations are available in the "HER-with-PGMs" on Zenodo repository: https://doi.org/10.5281/zenodo.7706027.

Submitted 25 November 2022
Accepted 5 April 2023
Published 10 May 2023
10.1126/sciadv.adf9931